Energy Harvesting from Hydraulic and Vibration Sources

POLITECNICO DI TORINO

DEPARTMENT OF MECHANICAL AND AEROSPACE ENGINEERING

Ph.D. in Mechatronics

Ph.D. Thesis

Energy Harvesting from Hydraulic and Vibration Energy Sources

Nima Mohammad pour

Supervisor
Prof. Andrea Tonoli

Doctoral Course Coordinator
Prof. Giancarlo Genta

14 March 2014

Acknowledgements

Everything started in 2010 while I was working in a company. Thanks to my supervisor Prof. Andrea Tonoli I had the possibility to start a Ph.D. in Mechatronics at the Polytechnic of Turin. It was a big decision as I had to start the Ph.D. without any scholarship giving up the salary from the company I was working with. Regarding this, I would like to thank my father who helped me and supported me to make the right decision.

I am grateful to Dr. Joaquim Girardello Detoni, Dr. Renato Galluzzi, Diego Boero and the whole staff of the Mechatronics Laboratory of the Polytechnic University of Turin (LIM) for their support and kindness during my Ph.D. Furthermore, my deepest appreciation goes to the Autonomous region of Aosta Valley for their financial support during the last two years of my studies.

I would like to express my gratitude to Prof. Steve Beeby, who gave me the great possibility to do research abroad for 6 months at the University of Southampton, Electronic and Computer Science department. His advice and comments, as well as those given by Dr. Dibin Zhu and Dr. Russel Torah, have been a great help in the design and fabrication of piezoelectric energy harvesters. I can definitively say that during my Ph.D., the period abroad was the most productive from the research point of view and that is for sure because of these colleagues.

I am in debt to Ian Bedwell, because of his patience, kindness and perseverance in helping me in using Ansys Workbench. Every time I use Ansys, I recall his contribution and it will be never forgotten.

My deepest appreciation goes to Dr. Carlo Novara, who allowed me to cultivate my passion, in the field of biomedical engineering science. I have really appreciated the fact that he believed in my ideas helping me to make them reality.

A special thanks to my family. Words can not express how grateful I am to them for all of the sacrifices that they have done to allow me to achieve my goals.

I am deeply grateful to my girlfriend, Sonia Chessa, who shared with me all the difficulties that I encountered in these last few years, encouraging me to never give up.

Last but not least, I would like to thank all of my friends, that made these last years special, precious moments I will never forget.

Abstract

This doctoral thesis, is divided in two main parts. The first is about load optimisation for a hydraulic energy harvester while the second part focuses on the design and fabrication of piezoelectric energy harvesters for the single supply pre-biasing circuit. An abstract for each part is reported below:

- Part I: The hydraulic power available in water pipes is usually wasted while it could be harvested and used to supply low power systems. To address this shortcoming, this study presents how load matching allows to harvest the maximum hydraulic power available in the environment. The hydraulic energy harvester considered in this study is composed of a hydraulic turbine and a permanent magnet generator. To estimate the optimal external load that maximises the power transfer, first a mathematical model of the harvester is introduced and then validated with experimental test. The benefit of this study consists in harvesting the maximum hydraulic power available for any input flow rate without changing physical parameters of the hydraulic turbine and the permanent magnet generator. Experimental and Simulation results show that by using the optimal load, the power transferred is maximum and consequently maximized power on the external load is available.

- Part II: The design and test of a novel screen printed piezoelectric energy harvester for the single supply pre-biasing (SSPB) circuit is presented. It was demonstrated in previous research that by using the SSPB circuit, power delivered to the load was over three times greater than that in the case of using a bridge rectifier circuit. For maximum power extraction from energy harvesters using the SSPB circuit, the SSPB switches must be triggered when the piezoelectric beam reaches its maximum point of displacement. Therefore, an accurate peak detection sensor is required. A new piezoelectric energy harvester integrating a small piezoelectric area for peak detection with a larger piezoelectric area for energy harvesting was designed and fabricated. The difference in capacitance between the peak detection sensor and the piezoelectric energy harvesting component leads to a phase difference between the two outputs if the load impedance is low. This phase difference can cause the switches

to be fired at the wrong time and thus reduce the efficiency of the SSPB circuit. A mathematical model was developed to study the phase difference. It was found both in simulation and experiments that impedance matching can be performed in order to eliminate the phase difference.

Contents

Chapter 1

Introduction to energy harvesting

1.1 Background

Over the last few years, there has been a growing interest in energy harvesting (EH) devices to allow autonomous operation of control or monitoring devices. Energy harvesters convert a small amount of environmental energy, which is usually wasted, into electrical energy [1].Energy harvesters typically generate power levels on the order of μW to mW [1].

Energy harvesters are often used in order to make systems with low power consumption entirely autonomous. Consequently these systems do not need any power supply from the grid. The energy harvested costs nothing because energy harvesters capture residual quantities of energy that are usually wasted. Furthermore, energy harvesters create no carbon emissions and are therefore environmentally friendly. They may also be less expensive and easier to implement compared with traditional systems using non-rechargeable batteries or a mains supply because they do not need replacement as batteries would, or require cabling to the supply.

Energy storage is an important part of EH because the harvested power is usually variable in time and may not be high enough to directly supply the system when needed. Therefore, a storage element such as a rechargeable battery or a supercapacitor is necessary in order to guarantee a stable power supply to the load during periods in which the consumption exceeds the power supplied by the harvester. When a device does not need to be powered, the harvester uses the energy harvested to charge the storage element. However, for some specific applications (e.g. hydraulic energy harvester used by Bosch [2]), the battery is not needed because when the device needs to be supplied, the energy harvester is surely able to generate energy and supply the device. Therefore, during the design of an energy harvester, the availability of the source energy, its intensity and cost analysis should all be taken into account.

Figure1.1 shows the operating principle of energy harvesters. Energy sources

available in the environment could be in form of vibration, light, heat, etc. A transducer is necessary to convert the available environmental energy into electrical energy. Energy management is necessary to adapt the converted energy to supply the device directly or charge the storage element.

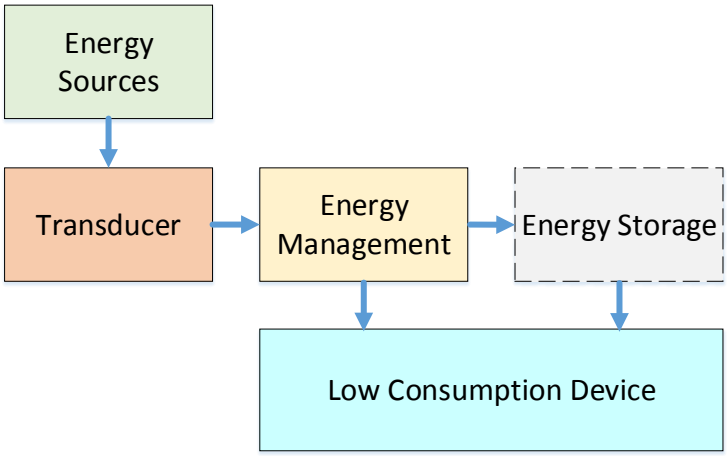

Figure 1.1. Generalized block diagram of an energy harvester operation principle.

Energy harvesters can be integrated directly into an autonomous system. This means that wiring could be avoided. Consequently, the system will be easier to install, lighter, cheaper and more suitable for mobile or remote applications.

Mechanical energy harvesters are more commonly used than those that use other sources, such as heat, light, magnetic fields, etc.. This is because greater output power is generated by mechanical energy harvesters compared to other types. Mechanical energy sources could be hydraulic, vibrational, pressure, force, etc.. In this thesis a hydraulic and a piezoelectric energy harvester are investigated. In both cases mechanical energy sources are converted to electrical energy.

1.2 Motivation

The main purpose of the studies performed is to increase the efficiency and output power density of hydraulic and piezoelectric energy harvesters. Two studies are undertaken:

1. The optimization of a hydraulic energy harvester composed of a hydraulic turbine and a permanent magnet generator.

2. Design, fabrication and experimental testing of novel piezoelectric energy harvesters for use with a single supply pre biasing circuit.

In both cases, simulation results are validated and compared with experimental results.

1.3 Scientific contribution

The two main scientific contributions arising from this work are summarized below:

1. For hydraulic energy harvesters composed of hydraulic turbines and permanent magnet generators, it was found that the maximum output power of the harvester is obtained for an optimum load, different from the impedance of the generator. Therefore, impedance matching with the generator does not achieve the maximum power as the hydraulic turbine modifies the optimum point of operation. A methodology that can be used to find the optimum load is described in the part one of the thesis.

2. A novel piezoelectric energy harvester is designed for use with a single supply pre biasing circuit (SSPB). In previous research, it was demonstrated that when using this circuit, the output power is three times greater than with a bridge rectifier circuit. Therefore, the design of this novel harvester with an integrated sensor for peak detection is relevant for the use of the SSPB circuit. A phase shift occurs between the generator voltage and the integrated sensor voltage which affects the operation of the SSPB circuit. Analytical and experimental results confirm that, in case of low impedance loads, impedance matching should be performed to avoid phase shift.

1.4 Thesis outline

The present doctoral dissertation is divided in ten chapters.

Chapter 1 The first chapter gives an introduction to energy harvesting. This chapter describes the aims of and motivation for this work and the scientific contribution.

Chapter 2 In the second chapter, hydraulic energy harvesters are introduced. This chapter will focus on hydraulic energy harvesters made of a hydraulic turbine and a permanent magnet generator.

Chapter 3 Chapter 3 presents the development of the mathematical models for the turbine and the permanent magnet generator. These models are used to detect the load impedance that provides maximum power in such a system. The methodology used is described and analysed in detail.

Chapter 4 In this chapter, simulation and experimental results (provided by using a commercial hydraulic energy harvester [2]) are compared to validate the study of hydraulic energy harvesters. Maximum power point tracking for variable input systems is described.

Chapter 5 In this chapter, the conclusions of the work on hydraulic energy harvesters are reported. Possibilities for future work are proposed.

Chapter 6 Chapter 6 introduces piezoelectric materials, cantilevered piezoelectric energy harvesters and the single supply pre biasing circuit.

Chapter 7 The design and simulation of the piezoelectric energy harvester is presented in this chapter. Design considerations are discussed and the finite element simulation of the device with Ansys Workbench is reported.

Chapter 8 This chapter describes the fabrication process and testing of the designed piezoelectric energy harvester.

Chapter 9 In this chapter, a mathematical model of the harvester is developed in order to study the phase shift between the harvesting and sensing voltages.

Chapter 10 The main findings of the work regard piezoelectric energy harvesters are summarized in this chapter. Possibilities for future research are discussed.

Part I

Load Optimisation for Hydraulic Energy Harvesters

Chapter 2

Introduction to hydraulic energy harvesters

Similarly to thermal and vibration energy harvesters, the interest in hydraulic energy harvesters is increasing. They can be realized using piezoelectric materials that move in a fluid [3–7] or by very small hydraulic turbines [2, 8–10]. There are several household applications (such as electronic tap sensors) of these systems in bathrooms where sensors (that control valves) are powered by the energy harvested by hydraulic turbines [8]. Same systems are also proposed to supply thermostatic valves [9] , LEDs in shower heads [10] or boilers during the ignition phase [2]. These harvesters could also be used in smart buildings to harvest energy from the water used by inhabitants, during everyday activities.

In hydroelectric power stations, gates are often used to regulate the flow rate because usually the turbines and the generators are designed to work with a nominal flow rate [3, 11–13]. The nominal power is guaranteed when the flow rate is equal to or greater than the rated flow. The advantage of the proposed technique consists in transferring the maximum power to the load for any value of input flow rate without changing the physical parameters of the turbine and generator.

The aim of this study is to model a system that is able to: 1) harvest hydraulic energy and 2) optimise the electrical load as a function of the input flow rate, to maximise the harvested power in hydraulic energy scavengers composed of a hydraulic turbine connected to a permanent magnet generator. Firstly the system is described; then a mathematical model of the hydraulic turbine and one of the generator are used to detect the optimum load that maximises the harvested power. Finally experimental test are performed to validate simulation results and the effectiveness of the study.

The harvester modelled for this study is available in commerce (product code: J8707406104) and is fabricated by Junkers Bosch [2]. The harvester is positioned

in a boiler and used for its ignition. As shown in Figure 2.1, the conversion unit is composed of a hydraulic cross flow turbine and a permanent magnet generator.

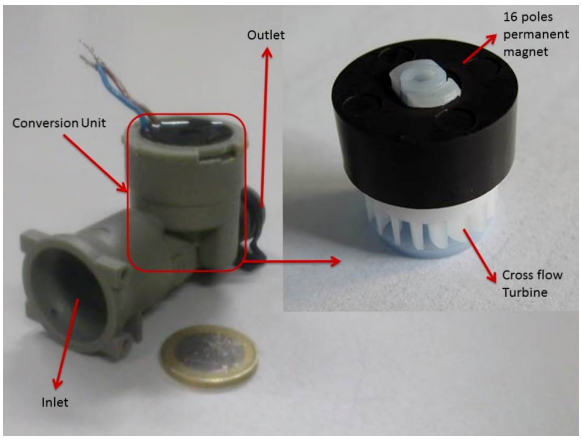

Figure 2.1. Hydraulic energy harvester (product code: J8707406104)

Chapter 3

Mathematical modelling of the hydraulic energy harvester and maximum power point detection

The goal of this section is to describe how to track the maximum power point of the hydraulic scavenger to cope with a variable input flow rate (Q_{in}). The efficiency of the scavenger is given by the product of the hydraulic turbine efficiency and the generator efficiency. As the input or the load changes, the system operating point is not constant with implications in the efficiency of the scavenger. The aim is to adapt the load to maximise the power available for any value of the input flow rate. Here, a mathematical model of the harvester is used for the efficiency estimation of the turbine and the generator. Figure 3.1 illustrates the scheme of

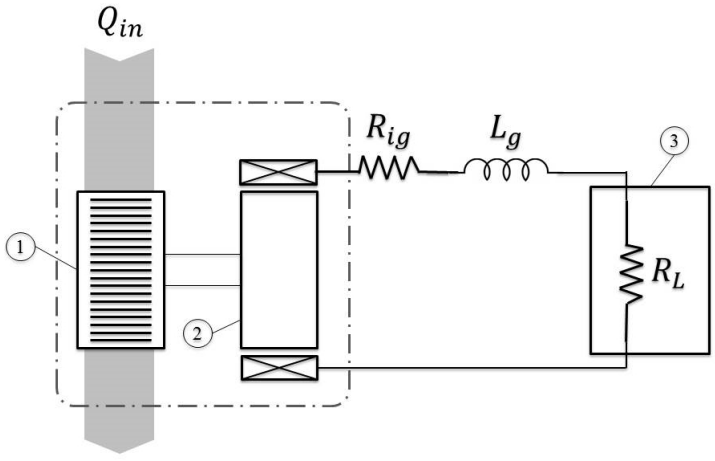

Figure 3.1. Simplified scheme of the energy harvester. Hydraulic turbine (1), Electric machine (2), Output load (3).

the system highlighting the internal resistance of the generator winding (R_{ig}), the armature reaction (L_g), the input flow rate (Q_{in}) and the output load (R_L). In case a battery or a circuit is connected to the harvester, (R_L) would represent its equivalent impedance.

The turbine and generator models are illustrated below and then joined together to study the efficiency of the scavenger.

3.1 Turbine model

The energy available in a flow is the sum of kinetic, potential and pressure energies (Bernoulli). In few domestic applications currently available on the market, small turbines are usually installed in line with the pipe with negligible head so that the turbine can not benefit from the potential energy of the flow. As the cross flow turbine is an impulse type one, the pressure energy is converted into kinetic energy at the inlet (by the reduction of the water jet area in the nozzle). Hence, only the kinetic energy is considered during the estimation of the input power and, considering the flow incompressible, the input power can be written as:

$$P_h = \frac{1}{2}\dot{m}{V_1}^2 \tag{3.1}$$

where V_1 is the absolute velocity of the inlet flow and $\dot{m}$ is the mass flow rate. Figure 3.2 [14] shows the velocity triangles in a cross flow turbine. It could be seen that there are two stages and in each stage the flow acts on a blade transferring energy. Therefore, the inlet and outlet velocities in each stage are different. Vectors named U represent the tangential velocities of the turbine in points 1, 2, 3 and 4. Obviously, $U_1 = U_4$ and $U_2 = U_3$. Vectors named V and W are the absolute and relative velocities of the fluid, respectively. The α angles are the angles between the tangential and absolute velocities while the β angles are those between the tangential and relative velocities. It is possible to assume [15]:

$$\begin{aligned} \alpha_2 &= \alpha_3 \\ \beta_2 &= \beta_3 \\ \beta_1 &= \beta_4 \end{aligned} \tag{3.2}$$

since they are corresponding angles of the same blade.

Relative velocities W_1 and W_4 are related through a coefficient ϕ which is an empirical coefficient less than unity (about 0.98) that takes into account the losses due to the friction of the flow in the nozzle and on the blades:

$$W_4 = \phi W_1. \tag{3.3}$$

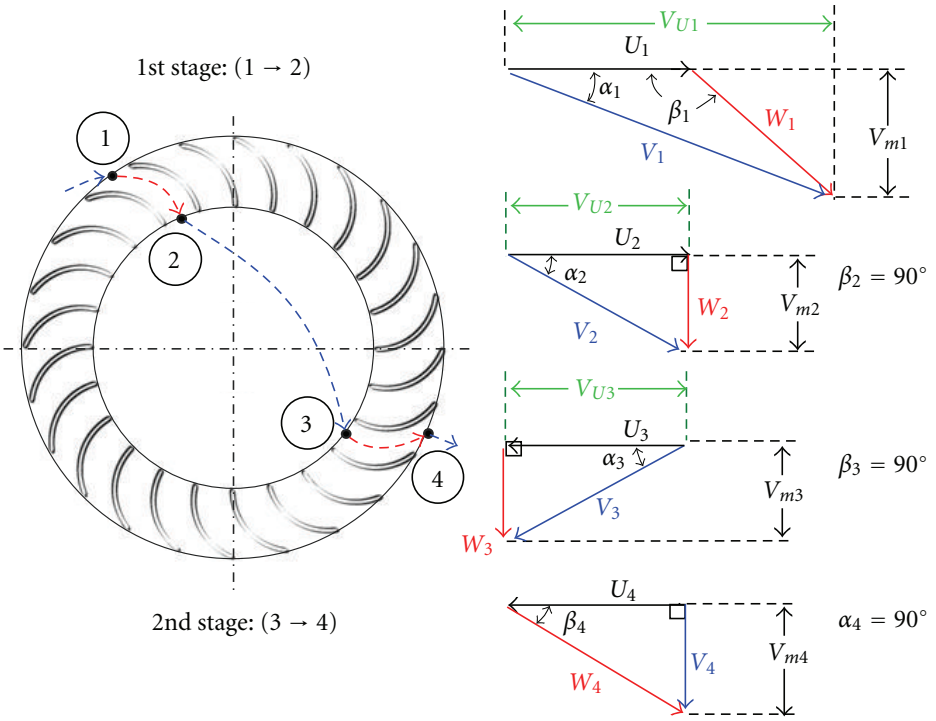

Figure 3.2. Cross flow turbine scheme and velocity triangles: Tangential velocity of the turbine (U), Absolute velocity of the flow (V) and Relative velocity of the flow (W) [14].

The force applied by the flow to a blade is equal to the mass flow rate multiplied by the change in velocity of the flow before and after crossing it. In the case of a cross flow turbine, the force applied to the blades is equal to:

$$F = \dot{m}(V_1 \cos\alpha_1 + V_4 \cos\alpha_4). \tag{3.4}$$

Therefore, the power output power of the turbine is:

$$P_o = F \cdot U_1 = U_1 \dot{m}(V_1 \cos\alpha_1 + V_4 \cos\alpha_4). \tag{3.5}$$

From figure 3.2, it can be seen that:

$$\begin{aligned} V_4 \cos\alpha_4 &= W_4 \cos\beta_4 - U_1 \\ W_1 \cos\beta_1 &= V_1 \cos\alpha_1 - U_1. \end{aligned} \tag{3.6}$$

Consequently the power is equal to:

$$\begin{aligned} P_o &= U_1\dot{m}(V_1\cos\alpha_1 + V_4\cos\alpha_4) \\ &= U_1\dot{m}(V_1\cos\alpha_1 + W_4\cos\beta_4 - U_1) \\ &= U_1\dot{m}(V_1\cos\alpha_1 + \phi W_1\cos\beta_1 - U_1) \\ &= U_1\dot{m}(V_1\cos\alpha_1 + \phi(V_1\cos\alpha_1 - U_1) - U_1) \\ &= U_1\dot{m}(V_1\cos\alpha_1 + \phi V_1\cos\alpha_1 - \phi U_1 - U_1) \\ &= U_1\dot{m}(V_1\cos\alpha_1 - U_1)(1 + \phi\frac{\cos\beta_4}{\cos\beta_1}). \end{aligned} \tag{3.7}$$

Thus, the efficiency is:

$$\begin{aligned} e = \frac{P_o}{P_h} &= \frac{U_1\dot{m}(V_1\cos\alpha_1 - U_1)(1+\phi)}{\frac{1}{2}\dot{m}{V_1}^2} \\ &= \frac{2U_1}{V_1}(\cos\alpha_1 - \frac{U_1}{V_1})(1+\phi). \end{aligned} \tag{3.8}$$

The maximum efficiency can be calculated as reported below:

$$\begin{aligned} \frac{de}{d\frac{U_1}{V_1}} &= 2(1+\phi)\left[\frac{de}{d\frac{U_1}{V_1}}\left(\frac{U_1}{V_1}\cos\alpha_1 - \frac{{U_1}^2}{{V_1}^2}\right)\right] \\ &= 2(1+\phi)\left[\cos\alpha_1 - 2\frac{U_1}{V_1}\right] = 0 \end{aligned} \tag{3.9}$$

and it can be found that the maximum efficiency is reached when:

$$U_1 = \frac{1}{2}V_1\cos\alpha_1. \tag{3.10}$$

By substituting equation 3.10 in equation 3.8, the maximum efficiency is equal to:

$$e_{max} = \frac{1}{2}\cos^2\alpha_1(1+\phi). \tag{3.11}$$

It is possible to rewrite the equation 3.8 in terms of the volume flow rate Q_{in}, The turbine angular velocity ω_t, the outer radius of the turbine r and the area of the water jet in input a:

$$e = 2\frac{\omega_t r a}{Q_{in}}(\cos\alpha - \frac{\omega_t r a}{Q_{in}})(1+\phi). \tag{3.12}$$

It can be noticed from equation 3.12 that the efficiency is a function of the input flow rate Q_{in} and the turbine angular velocity ω_t. Therefore, the efficiency can be

calculated with respect to the turbine angular velocity at different input flow rates. Figure 3.3 illustrates that each input flow rate generates a different efficiency curve and each of these curves shows how the efficiency changes with respect to the turbine angular velocity. For a constant input flow rate, the efficiency reaches its maximum value when the turbine works at its nominal angular velocity as specified during the design of the turbine. Figure 3.3 shows that increasing the flow rate, the speed corresponding to the maximum efficiency increases. In order to reach the maximum efficiency point while the input flow is changing, it is necessary to regulate the speed of the turbine.

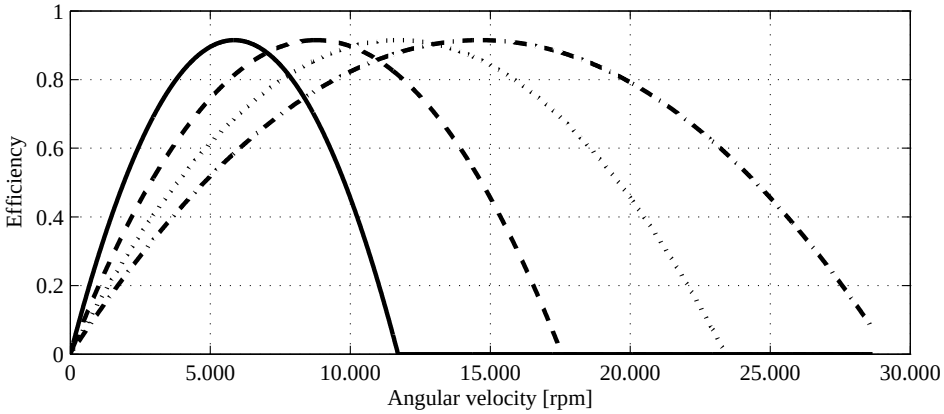

Figure 3.3. Cross flow turbine efficiency at different input flow rates Q_{in}: Solid line = 2 [l/min]; Dashed line = 3 [l/min]; Dotted line = 4 [l/min]; Dash-dotted line = 5 [l/min].

The turbine input and output power are going to be defined and substituted in equation 3.12 in order to obtain the turbine output torque. The output power of the hydraulic turbine is equal to:

$$P_{ot} = T_t \omega_t \tag{3.13}$$

where T_t is the torque generated by the turbine. Considering equation 3.12, the torque can be written as:

$$T_t = \frac{\rho r Q_{in}^2}{a}(\cos\alpha - \frac{\omega_t r a}{Q_{in}})(1+\phi) \tag{3.14}$$

The losses inside the hydraulic turbine are taken into account in the efficiency equation (**??**) and those related to the mechanical friction affecting the rotor shaft are modelled as a resistive torque T_r proportional to the generator's angular speed ω_g that acts against the turbine [16]:

$$T_r = C_m \omega_g \tag{3.15}$$

where C_m is a viscous loss coefficient. Thus, the turbine output torque can be written as:

$$T_d = T_t - T_r. \tag{3.16}$$

The output of the turbine is expressed in terms of a torque in order to compare it with the torque required by the generator. This will allow us to find the optimal operation point.

3.2 Generator model

The electric generator can be modelled as a single-phase synchronous machine in steady state condition. The right part of Figure 3.1 shows the equivalent circuit of the generator. Its output voltage could be expressed as:

$$|\overrightarrow{E}| = k_e \cdot p \cdot \omega_g \tag{3.17}$$

Where E is the absolute value of the voltage generated, k_e is the generator voltage constant, p is the number of pair of poles and ω_g is the angular velocity of the generator. The absolute value of the generator's impedance is:

$$|\overrightarrow{Z}| = \sqrt{(R_{ig} + R_L)^2 + (p \cdot \omega_g \cdot L_g)^2}. \tag{3.18}$$

The current that flows in the circuit is then:

$$|\overrightarrow{I}| = \frac{k_e p \omega_g}{\sqrt{(R_{ig} + R_L)^2 + (p \cdot \omega_g \cdot L_g)^2}}. \tag{3.19}$$

The real power generated by the generator is equal to:

$$P_{og} = |\overrightarrow{E}|^2 \cdot |\overrightarrow{I}|^2 \cdot \cos\beta \tag{3.20}$$

where β is the phase angle between the current and voltage sine waves:

$$\cos\beta = \frac{R_{ig} + R_L}{\sqrt{(R_{ig} + R_L)^2 + (p * \omega_g * L_g)^2}}. \tag{3.21}$$

Considering the generator lossless, the following equation could be written:

$$\omega_g \cdot T_g = |\overrightarrow{E}|^2 \cdot |\overrightarrow{I}|^2 \cdot \cos\beta \tag{3.22}$$

where T_g is the torque required by the generator and can be expressed as:

$$T_g = \frac{k_e^2 \cdot p^2 \cdot \omega_g}{(R_{ig} + R_L)\left[1 + \left(\frac{p \cdot \omega_g \cdot L_g}{R_{ig} + R_L}\right)^2\right]}. \tag{3.23}$$

3.3 Maximum power point detection

At steady state the torsional equation condition of the rotor shaft states that:

$$T_d = T_g. \tag{3.24}$$

Figure 3.4 illustrates the torques required by the generator for few load values and the output torque produced by the turbine. It could be noticed that each load, forces the harvester to work at a different angular velocity. Consequently the output power produced by the harvester changes as a function of the external load. It is possible to calculate the output power at each point where $T_g = T_d$ and choose the output load that allows us to reach the highest output power.

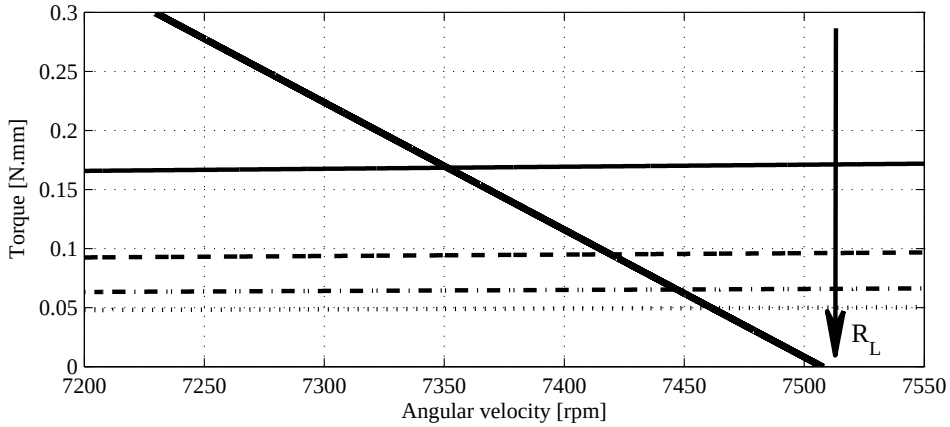

Figure 3.4. Torques versus angular velocity: Thin solid line (T_g) $R_L = 50$ [Ω]; Dashed line (T_g) $R_L = 100$ [Ω]; Dash-dotted line (T_g) $R_L = 150$ [Ω]; Dotted line (T_g) $R_L = 200$ [Ω]; Thick solid line $T_t - T_r$; $Q_{in} = 4$ [l/min].

If the flow rates changes, the angular velocity of the turbine changes and the optimum load changes too. Therefore, if the system has a variable input, a variable load is needed to track the maximum power point. Figure 3.4 shows how the optimum point changes by varying the external load.

Chapter 4

Testing of the hydraulic energy harvester

The experimental test is performed by the harvester illustrated in Figure 2.1. The parameters of the harvester are measured and listed in table 4.1.

Parameter	Description	Value
r	Radius of the turbine	$5[mm]$
a	Approximate nozzle area	$5.22[mm^2]$
p	Number of pairs of poles of the generator	8
R_{ig}	Internal resistance of the generator winding	$2.18[\Omega]$
L_g	Inductance of the generator winding	$3.11[mH]$
k_e	Generator constant voltage	$0.00045[\frac{V \cdot s}{rad}]$

Table 4.1. Parameters of the hydraulic energy harvester (J8707406104)

Figure 4.1 illustrates how the experimental test is done: the flow rate is set at a constant value $Q_{in} = 4[L/min]$ by using a flow meter connected to the first channel of an oscilloscope where the frequency of the signal generated by the flow meter is observed. From the data sheet of the flow meter, it could be seen that the frequency of the signal generated is related to the flow rate. Then, an external load is applied to the harvester that is connected to the second channel of the oscilloscope where the output voltage on the load is observed. By changing the external load connected directly to the generator, the voltage on it and the power generated by the harvester change. Figure 4.2 illustrates that the maximum power is achieved when the external load is equal to 22Ω.

A simulation is performed in order to estimate the optimal load and verify that by using it, the power transferred reaches its maximum. The parameters of the

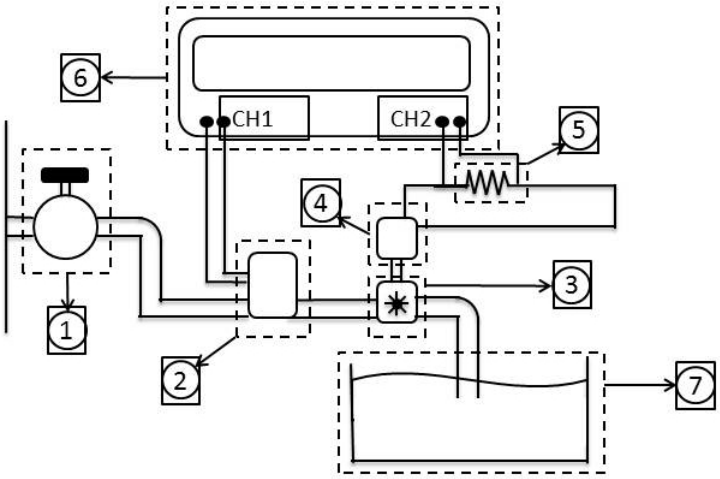

Figure 4.1. Schematic of the test bench for experimental results: tap (1); Flow meter (2); Hydraulic turbine (3); Permanent magnet generator (4), External resistive load (5), Oscilloscope (6).

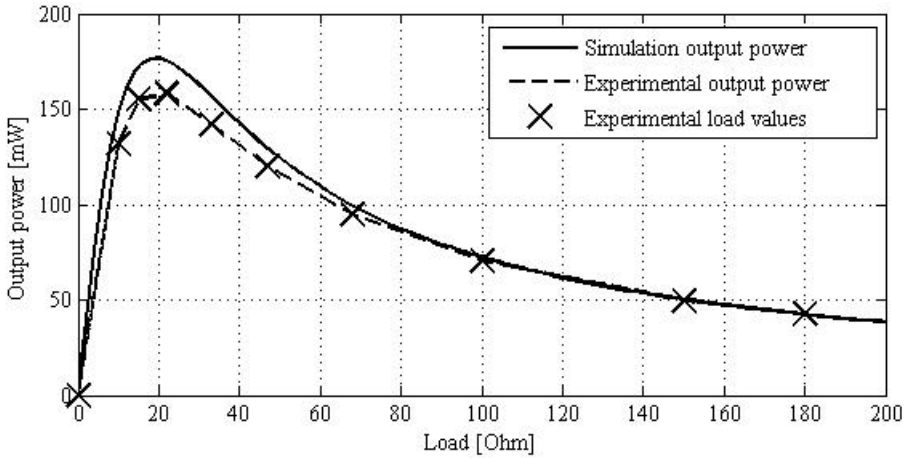

Figure 4.2. Output power with respect to the external load: $Q_{in} = 4$ [l/min].

simulation are set as the experimental test. The generator viscous coefficient is identified experimentally and is equal to $C_m = 7 \cdot 10^{-6}[Nms]$.

Figure 4.2 shows that the generated power is a function of the external load. Simulation result confirm that the maximum power point is reached for an external load equal to $R_L = 19.3\Omega$. Table 4.2 compares results of experimental test and simulations.

Results	Experimental	Simulation
Optimum External load	22Ω	19.3Ω
Optimum Angular velocity	7123.8 [rpm]	$7355.15[rpm]$
Maximum Output power	$158[mW]$	$179.1[mW]$

Table 4.2. Comparison of experimental and simulation results

The differences between the simulation and experimental results has several reasons. First of all, the flow rate is considered constant in the simulation while in the experimental test it had small variations in time. Furthermore, errors due to the measurement of the flow by the flow meter should be considered. Moreover, in the simulation the load values are with a higher resolution while during the experimental test few resistances with discrete values are used. However, the comparison of results validate the mathematical model of the harvester and consequently it can be used to estimate the optimal load value.

The generator has an impedance equal to $|\overrightarrow{Z}| = 4.8\Omega$ and theoretically the power generated is fully transferred when $|\overrightarrow{Z}| = R_L$. However, it can be noticed how the turbine influences the functioning of the system so that the optimum load is different from the nominal load able to transfer all the power generated.

Figure 4.3 shows how the optimal value of the external load changes with respect to the input flow rate. Therefore, if the input flow rate changes, an optimal value of the external load can be found in order to always have the maximum output power. In other words, it is possible to track the maximum power point of the system for any value of the flow rate.

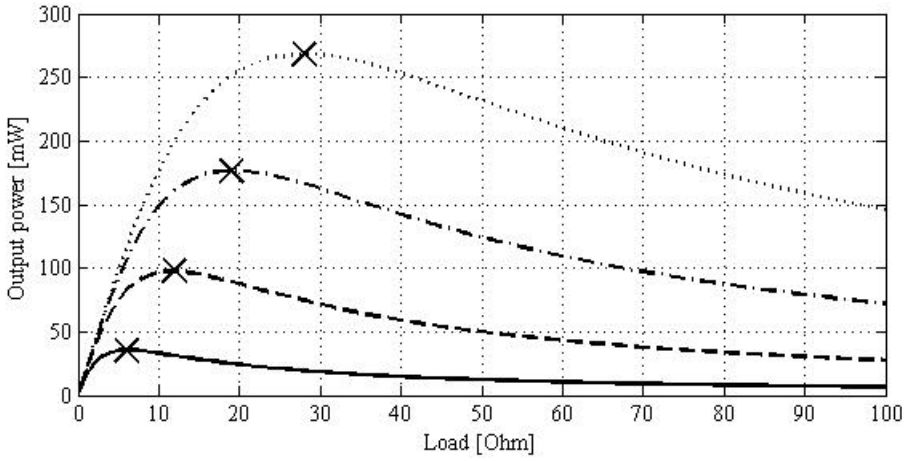

Figure 4.3. Output power versus to the external load for variable input system: Solid line Q_{in} = 2 [l/min]; Dashed line Q_{in} = 3 [l/min]; Dash-dotted line Q_{in} = 4 [l/min]; Dotted lineQ_{in} = 5 [l/min].

Chapter 5

Conclusions

It has been shown how the external laod connected to hydraulic energy harvesters composed of a hydraulic turbine and a permanent magnet generator affect the output power generated by the scavenger. It has been demonstrated that the optimum load that maximises the output power is different from the generator's impedance since the the hydraulic turbine affect the optimal operating point of the harvester.

Furthermore, this study proves that a variation of the input flow rate, causes a change of the optimum load that maximises the output power. Therefore, when the input flow is variable in time, output load tuning allows to track the maximum power point without changing the physical parameters of the hydraulic turbine and the permanent magnet generator.

Further work could be done on the design of the energy storage unit and how this will affect the efficiency and the power transfer of the hydraulic energy harvester.

Part II

Design and Experimental Validation of a Piezoelectric Energy Harvester for Single Supply Pre-Biasing Circuit

Chapter 6

Introduction to piezoelectric materials and piezoelectric energy harvesters

Energy harvesting is the process of capturing and storing energy from ambient energy sources. Mechanical vibration energy harvesters are receiving increasing interest as an alternative power source to batteries for autonomously operating devices because of their longer lifetime, lower cost and lower environmental impact. The three main transduction methods used to convert mechanical vibration energy into electrical energy are electromagnetic, electrostatic and piezoelectric transducers [17]. Over the past decade, piezoelectric transducers have received special attention due to their simplicity in structure, which makes them easy to integrate into self powered systems.

6.1 Introduction to piezoelectric materials

To understand piezoelectricity and how piezoelectric materials are defined, it is necessary to review the classification of materials based on conductivity. An elementary classification involves dividing materials into two groups: conductors that allow the flow of electric charge in one or more directions and insulators which internal electric charges do not flow freely. Dielectric materials are insulators which can be polarized when an external electric field is applied. The polarization of the material consists of the displacement of its cations and anions due to an external electric field. This causes changes in dimensions of the material. Conversely, when an external stress is applied to a dielectric material, it accumulates electric charge. This property is called piezoelectricity. The piezoelectric effect describes the electromechanical interaction between the mechanical stresses and electrical fields in a

piezoelectric material. The direct piezoelectric effect (generator effect) occurs when external mechanical stresses are applied to a piezoelectric material and as a result an electric field is induced in the material. The indirect piezoelectric effect takes place when electrical fields are applied across the piezoelectric material and as a result the body generates mechanical stresses and deforms. Therefore, a piezoelectric can be thought of as a transduction system able to convert the electrical energy into mechanical or vice versa. The electric variables are surface charge density (D), electric field (E), while the mechanical variables are in the form of strain (x) and stress (X). The coefficients that relate the input and output parameters describe the sensitivity of the piezoelectric material and are described in the following section.

6.1.1 Piezoelectric coefficients

To understand the meaning of the piezoelectric coefficients, it is necessary to define the relationship between flux density D and the electric field E. When an electric field E is applied to a dielectric material, the material develops a finite polarization P and an internal electric flux density D. The relationship between thesis defined in the following equation:

$$\overrightarrow{D} = \varepsilon_0 \overrightarrow{E} + \overrightarrow{P}. \tag{6.1}$$

The coefficients that link the mechanical to the electrical variables are listed in table 6.1.

Operation mode	Input	Output	Equation	Coefficient	Unit
Direct	Strain	Flux density	$D = ex$	e	C/m^2
Direct	Strain	Electric field	$E = hx$	h	V/m
Direct	Stress	Flux density	$D = dX$	d	C/N
Direct	Stress	Electric field	$E = gX$	g	Vm/N
Indirect	Electric filed	Stress	$X = e^*E$	e^*	N/Vm
Indirect	Flux density	Stress	$x = h^*E$	h^*	N/C
Indirect	Electric filed	Strain	$X = d^*D$	d^*	m/V
Indirect	Flux density	Strain	$x = g^*D$	g^*	m^2/C

Table 6.1. Description of inputs, outputs and coefficients of a piezoelectric material in direct and indirect operational mode.

By using the identity $V = Nm/C$, it can verified that the pairs d,d^*,g,g^*,e,e^*,h,h^* have the same unit. Furthermore, from thermodynamics, it can be proved that [18]:

$$d = d^*, g = -g^*, e = -e^* \text{and } h = h^*. \tag{6.2}$$

The piezoelectric parameters are not absolute. Therefore, when a parameter is observed, the value indicates the change in the parameter. Consequently, the piezoelectric coefficients are more appropriately defined by partial derivatives. Another

important point is that when the output is the electric flux density, the electric field is considered fixed and vice versa. In the same way, when the output is strain, the stress on the material is considered fixed and vice versa. In addition to these four coefficients, there are three other parameters that affect the dynamics of a piezoelectric material. These parameters are the permittivity ε, the stiffness constant c and the compliance constant s.

In the direct piezoelectric effect, two conditions can arise. In the first case, the material is not mechanically constrained, so it is able to change dimensions under an applied field. In this case, the stress is constant and the governing condition is:

$$D = dX + \varepsilon^X E \tag{6.3}$$

where ε^X is the permittivity at constant stress.

In the second case, the material is clamped. In this case the material is not able to respond to a changing magnetic field. The strain is constant and the governing equation is:

$$D = ex + \varepsilon^x E \tag{6.4}$$

where $\varepsilon^X x$ is the permittivity at constant stain.

In the indirect piezoelectric effect, two conditions also arise. In the first case, the material is short circuited and the electric field is considered constant. The governing equations are:

$$\begin{aligned} x &= dE + s^E X \\ X &= -eE + c^E x \end{aligned} \tag{6.5}$$

where s^E and c^E are the elastic compliance and the elastic stiffness under constant electric field. In the second case, the material is open circuit and the charge density is constant. The governing equations are:

$$\begin{aligned} x &= gD + s^D X \\ X &= -hD + c^D x \end{aligned} \tag{6.6}$$

where s^D and c^D are the elastic compliance and the elastic stiffness under constant charge density.

6.1.2 Tensor form of piezoelectric equations

The permittivity, the piezoelectric coefficients, the elastic compliance constant and the elastic compliance constant are all tensors because they relate vectors and tensors. Tensors of second or higher rank usually use the reduced matrix notation,

where for simplicity, the two indices of the tensor i and j (each taking values 1 to 3), are replaced by a single index that takes values 1 to 6 [18]:

$$11 = 1;\ 22 = 2;\ 33 = 3;\ 23 = 32 = 4;\ 31 = 13 = 5;\ 12 = 21 = 6. \tag{6.7}$$

As these matrices are symmetric, they have few independent elements. Furthermore, the piezoelectric materials used in energy harvesting are poled in a specific direction and consequently they lose their isotropic nature and become orthotropic. Therefore, the number of independent components in these matrices is greatly reduced [18]. Table 6.2 shows the coefficients of a piezoelectric material and the dimensions of the matrices in tensor form.

Input	Output	Coefficient	Coeff. Matrix Dimen.	Numb. of ind. elements
x	D	e	$[3 \times 6]$	3
x	E	h	$[3 \times 6]$	3
X	D	d	$[3 \times 6]$	3
X	E	g	$[3 \times 6]$	3
E	X	e^*	$[6 \times 3]$	3
D	X	h^*	$[6 \times 3]$	3
D	x	d^*	$[6 \times 3]$	3
D	x	g^*	$[6 \times 3]$	3

Table 6.2. Description of the coefficients of a piezoelectric material and the dimensions of the matrices in tensor form.

The tensor form representation and the dimensions of the matrices describing the relationship between the elastic stiffness constant, the elastic compliance constant and the permittivity are given in table 6.3:

Input	Output	Coefficient	Coeff. Matrix Dimen.	Numb. of ind. elements
x	X	c	$[6 \times 6]$	4
X	x	s	$[6 \times 6]$	4
E	D	ε	$[3 \times 3]$	2

Table 6.3. Description of the coefficients of a piezoelectric material and the dimensions of the matrices in tensor form.

Regard the piezoelectric coefficients, the independent elements have indices 13, 15, 31, 33 and 51. Elements in position 13 and 15 are equal to elements in position 31 and 51. Regard the elastic stiffness coefficient and the elastic compliance coefficients, the independent elements have indices 11, 22, 12, 21, 13, 31, 44, 55 and 66. Elements in position 11, 12, 13, 44 and 66 elements are respectively equal to elements in position 22, 21, 31, 55 and $2(element_{11} - element_{12})$ respectively. To what concern

the permittivity, the independent elements have indices 1, 2 and 3 where $\varepsilon_1 = \varepsilon_2$. The coefficients d_{33},d_{31} and d_{15} are very important in the design of energy harvesters. These coefficients relate the stress to the charge density developed in the direct operation mode for three different orientation of applied stress. Figure 6.1 shows the orientation of applied stress for these three coefficients.

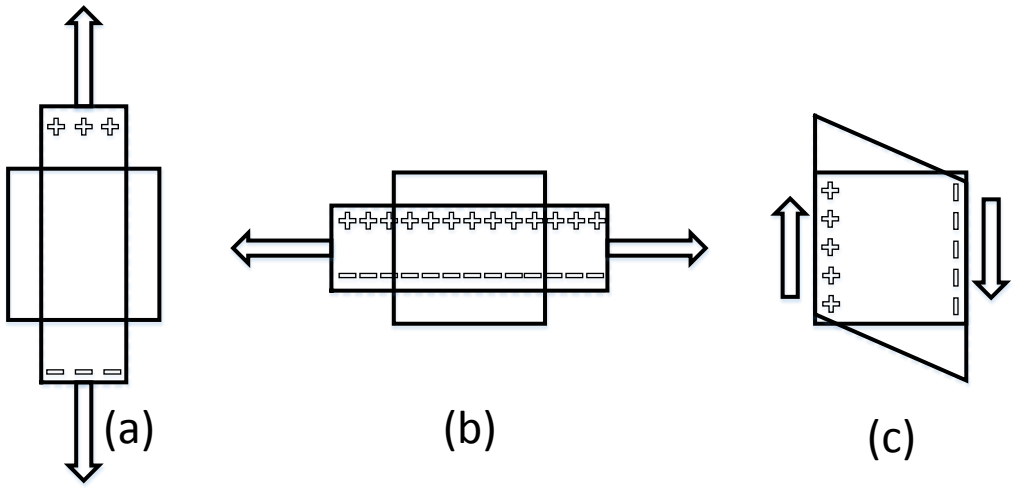

Figure 6.1. Direct piezoelectric effect: (a) Longitudinal mode d_{33}, (b) Transverse mode d_{31} and (c) Shear mode d_{15}.

6.1.3 Piezoelectric coupling coefficient

The electromechanical coupling coefficient, k_{ij}, is an indicator of the effectiveness with which the piezoelectric material converts the input energy into output energy. The first subscript to k denotes the electric field direction while the second denotes the direction along which the mechanical energy is applied or developed. It is defined as:

$$k_{ij}^2 = \frac{W_{em}}{W_e \times W_m} \tag{6.8}$$

where W_{em}, W_e and W_m are the piezoelectric, electrical and mechanical energy density respectively. From equations 6.3 and 6.5, the energy densities defined above

and the coupling coefficient can be written in terms of piezoelectric coefficients [18]:

$$\begin{aligned} W_{em} &= \frac{1}{2} dEX \\ W_e &= \frac{1}{2} \varepsilon^X E^2 \\ W_m &= \frac{1}{2} s^E X^2 \\ k^2 &= \frac{d^2}{\varepsilon^X s^E} \end{aligned} \tag{6.9}$$

k values depend on the design of the device, and orientation in which the stimulus is applied and the response is measured.

6.2 Introduction to cantilevered piezoelectric energy harvesters

The conversion of ambient energy in the environment into electrical energy by vibration piezoelectric energy harvesters can be described in three phases [19]. This process is illustrated in figure 6.2. The first phase is in the conversion of environ-

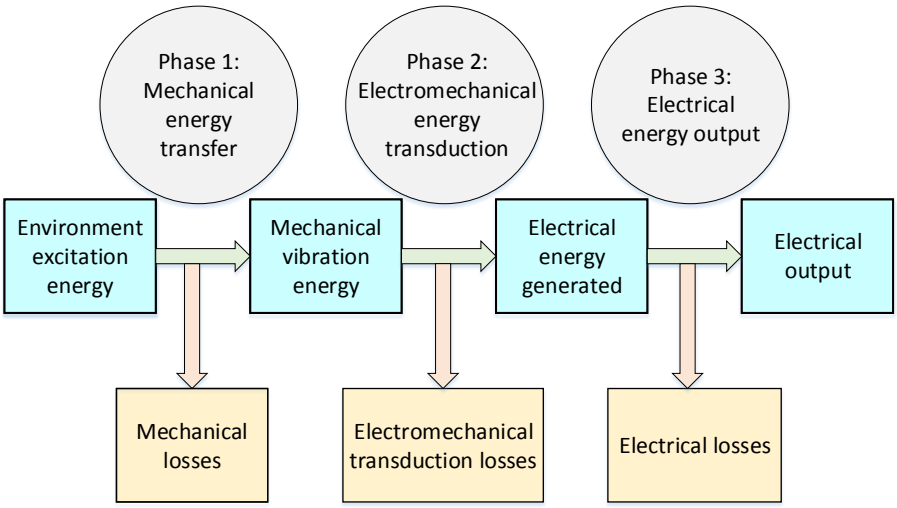

Figure 6.2. Energy flow for vibration piezoelectric energy harvesters.

mental excitation energy into cyclic oscillations through the mechanical assembly. During any energy conversion, part of the input energy is lost. In this first phase, losses are due to unmatched mechanical impedance, damping, and backward reflection. In the second phase, the cyclic mechanical oscillations are converted into cyclic

electrical energy. Energy is lost in this phase through electromechanical losses in the piezoelectric material. The coupling coefficient k determines the efficiency of this electromechanical conversion. In the third phase, the generated electrical energy is conditioned in order to supply the load. In this phase, losses are due to power consumption by the circuit.

Piezoelectric vibration energy harvesters are typically cantilever structures in which the piezoelectric material is attached to the top and bottom beam surfaces [17]. The structure's simplicity makes the harvester easy to integrate in a self powered system. The structure is designed to operate in one particular bending mode thereby straining the piezoelectric material and generating a charge in the d_{31} direction. The most common architectures used in energy harvesting are unimorph, bimorph or double layer bimorph cantilevers. Figure 6.3 shows the cross sections of the piezoelectric cantilevers with different structures. Each piezoelectric element,

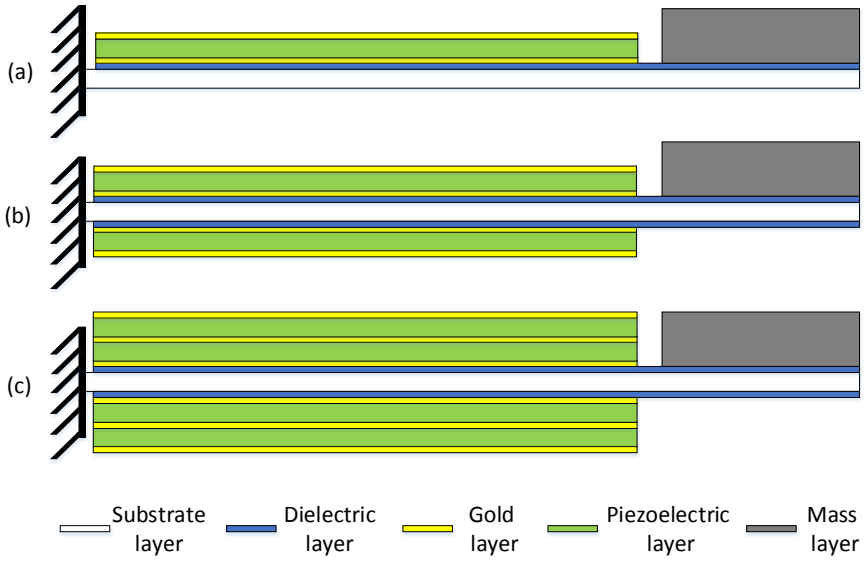

Figure 6.3. Piezoelectric cantilever structures: (a) Unimorph (b) Bimorph (c) Double layer bimorph.

can be connected to others in series or in parallel depending on the application. Figure 6.4 shows the circuit in the series case and the parallel case. In the series connection, the output voltage is doubled and the two piezoelectric are poled in the opposite direction. In the parallel connection, the two piezoelectric elements are poled in the same direction and the output power generated by the harvester is higher than the series configuration.

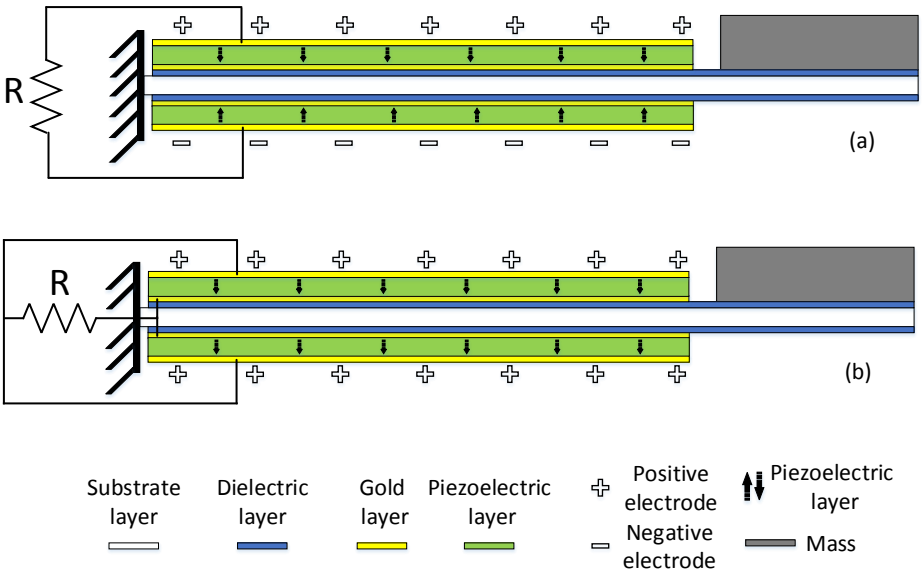

Figure 6.4. Series and parallel connections in piezoelectric cantilever structures: (a) Series connection (b) parallel connection.

6.3 Single supply pre-biasing circuit for piezoelectric energy harvesters

Several studies have been performed about power extraction circuit for piezoelectric energy harvesters [20]. The aims of these studies are:

- To achieve higher power density from the harvester by performing some form of impedance matching between the energy source, the transducer and the electrical system. This requires control of the input impedance of the circuit that interfaces to the transducer;
- To regulate the voltage in order to make the output current and voltage of the harvester compatible with the load electronics.
- To supply a storage element so that the intermittency of the energy harvesting source does not present continuous operation of the powered system.

Power extraction circuits for piezoelectric energy harvesters were compared in [21], which showed that the single supply pre-biasing (SSPB) circuit shown in figure 6.5, is the most suitable for low amplitude energy harvesting applications. The

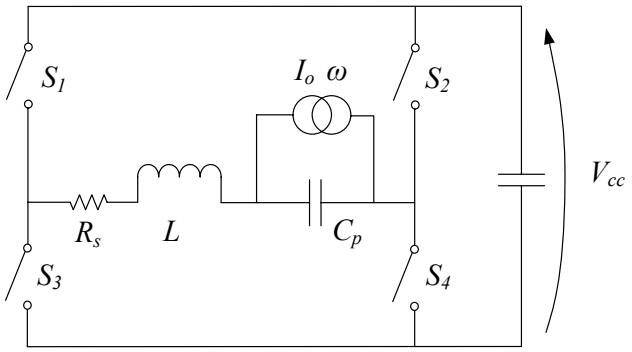

Figure 6.5. SSPB H-bridge circuit for discharging and pre-biasing the piezoelectric material [20].

SSPB circuit discharges and pre biases the piezoelectric beam using switches in an H-bridge configuration [20].

In [22], a multilayer piezoelectric harvester was tested with the SSPB circuit. Results showed that the power delivered to load is three times the power that a bridge rectifier circuit can provide. Figure 6.6 shows a comparison of the power output against the piezoelectric open voltage for devices with DC output.

Pre-biasing causes a stronger coupling between the electrical and mechanical systems [21] which improves efficiency. When a piezoelectric material is strained

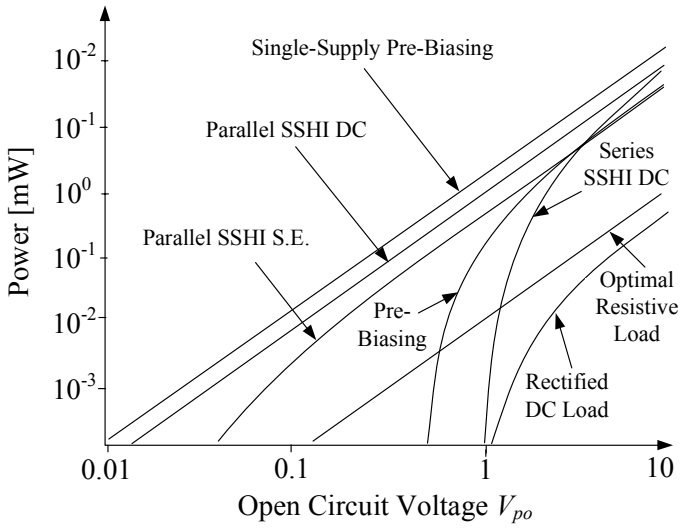

Figure 6.6. Comparison of circuits for energy harvesting devices with with DC output [20].

in one direction in open circuit configuration, the resulting charge displacement induces a force that tries to move the material back to an unstrained state, and some work is done in moving and deforming the material. If a charge is placed onto the material, forcing it to become deformed in one direction, before the material is forced to deform in the opposite direction by an external force, more mechanical work can be done as the effective stiffness of the piezoelectric material is increased. Therefore, more electrical energy can be generated.

When a piezoelectric cantilever is deformed upward at a maximum displacement, such that a positive charge would be generated by the downward deflection of the material if in an open circuit configuration, a negative pre bias voltage is applied to the material, allowing increased mechanical work to be done as the cantilever's free end moves downwards. The opposite applies when the free end of the piezoelectric cantilever is at the maximum downwards position.

To achieve maximum power extraction from the energy harvester, the switches must be triggered when the piezoelectric beam reaches its maximum point of displacement, which can be deflected using with the peaks and troughs of the voltage signal generated across piezoelectric material. Triggering early or late causes a drop in energy output [22], thus accurate peak detection is vital to achieving maximum power extraction.

Chapter 7

Design and finite element simulation of the piezoelectric energy harvester

In this chapter, the design and the finite element simulation of a novel cantilevered piezoelectric energy harvester suitable for use with the single supply pre biasing circuit is presented. The first part discusses the design and the structure of the harvester, while the second part focuses on its simulation.

7.1 Design of a novel cantilevered piezoelectric energy harvester for the SSPB circuit

As mentioned in the previous chapter, in an SSPB circuit, it is important that the pre biasing voltage is applied at the right moment. To achieve maximum power extraction from the energy harvester, the switches must be triggered when the piezoelectric beam reaches its maximum displacement, which coincides with the peaks and troughs of the voltage generated across a piezoelectric material. Triggering early or late causes a drop of energy output [22], thus accurate peak detection is vital to achieving maximum power extraction. One can use an external sensor to detect peaks. However, it increases complexity in the fabrication of energy harvesters. A piezoelectric sensing layer can be added to the harvester, however it must be electrically isolated from the generation layer, otherwise the sensing signal will be adversely affected by the pre-biasing charge [22]. In a single layer bimorph cantilevered energy harvester, one piezoelectric layer can be used for energy harvesting and the other can be used for sensing. However, in this case, only half of the total available capacitance can be used to harvest. In a double layer cantilevered energy harvester, only one of the four piezoelectric layers would be used to provide the sensing signal and thus three quarters of the total available piezo can be used for harvesting.

A new way to generate the piezoelectric sense signal involves in integrating an electrically isolated piezoelectric segment into the design of the piezoelectric harvester. The top-down and cross-sectional views of the harvester are shown in figure 7.1.

A T-shape bimorph cantilevered piezoelectric energy harvester is designed and shown in figure 7.1.

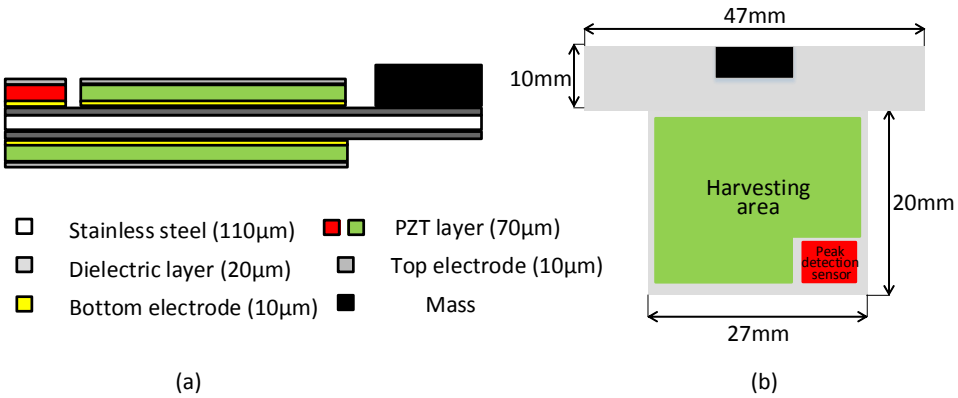

Figure 7.1. T-shape cantilevered piezoelectric energy harvester fo SSPB circuit: (a) Cross sectional view (b) Top view.

It could be seen that the mass is condensed along the direction of the width of the cantilever rather than the span. In this way, the tip displacement can be reduced to meet the power requirement within the size constraints [23].

In the cross-section view of figure 7.1, it can be seen that the bimorph harvester has different layers. The substrate is made of stainless steel and covered by glass. The glass is dielectric so it isolates the bottom electrode made of gold, from the substrate. The piezoelectric layer is placed between the gold bottom electrode and the top electrode, made of silver. The tungsten mass is fixed at the end of the cantilever and can be attached, allowing further experimention with different masses to be performed.

The peak detection area is on the top of the cantilever and positioned in the lower right corner to simplify its connection to the electrodes. Furthermore, as its position is near the clamping area, more stress is applied in the material and a higher voltage is generated. The RMS amplitude of the voltage generated by the peak detection sensor should be higher than $1.8V$ [22].

7.2 Finite element simulation of a cantilevered piezoelectric energy harvester for the SSPB circuit

The performance of the designed piezoelectric energy harvester is simulated using Ansys Workbench with direct coupled field analysis and a coupled physics circuit Ansys simulation. The setup and results of the simulation are described in sections 7.2.1 to 7.2.6.

7.2.1 Simulation set up

The first step in the simulation of piezoelectric energy harvesters is selecting the type of analysis needed to perform the simulation. As the energy harvester is cantilevered it is necessary to find the natural frequency of the structure, because maximum power is achieved when the system is excited at that frequency. Therefore the first analysis that should be performed is the modal analysis. A modal analysis determines the vibration characteristics (natural frequencies and corresponding mode shapes) of a structure. However, this analysis is not sufficient to predict the output voltage generated by the harvester at its resonant frequency. For this kind of study, harmonic response analysis should be used. In a structural system, any sustained cyclic load will produce a sustained cyclic (harmonic) response. Harmonic analysis results are used to determine the steady-state response of a linear structure to loads that vary sinusoidally (harmonically) with time, thus enabling verification whether or not the design will fail due to resonance, fatigue, or other harmful effects of forced vibrations. With a piezoelectric energy harvester, the input excitation will be mechanical vibration and the output is the voltage generated.

7.2.2 Definition of the materials

It should be noted that to define the coefficients and matrices of the piezoelectric material, codes should be used during the model set up as shown in the following sections.

7.2.3 Geometry definition

The harvester geometry can be imported from other CAD software or be input directly using the design modeller. As the harvester has different components, importing it from other software means that it is necessary to define all the connections between parts before performing the simulation. By using the design modeller, the system can be designed in two main ways. The first way involves designing each layer by creating different parts and then defining connections between them, while

the second method uses primitive functions. Primitive functions allow the system to be designed as a single part but with different bodies. The advantage of defining the system as a single part is that the connections do not require to be defined. Figure 7.2 shows the harvester designed with the design modeller by using the primitive functions. The dimensions of the sensing piezoelectric part are set $3 \times 3mm$ to find whether if this quantity of piezoelectric material is enough to generate $1.8V$.

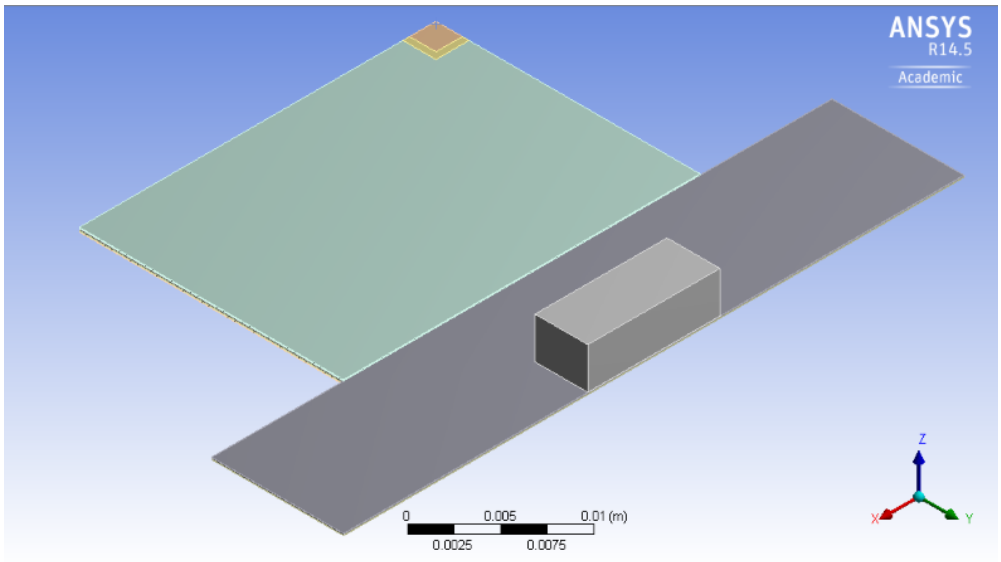

Figure 7.2. Geometry definition in design modeller (the top electrode is hid)

7.2.4 Model definition

It is necessary to define all the coefficients of the piezoelectric material. This is performed by adding commands in APDL language related to each part of the harvester model. During the definition of the piezoelectric material, the polarization direction is set and it is important to verify that the axes of the piezoelectric material are designed with coordinate system used in the model. If they are not aligned, it is possible to define the piezoelectric material polarization in the direction of another axis or define a new coordinate system.

As the system is modelled as a single part, it is not necessary to define the connections between the layers. The mesh is set automatically while different named selections are created. Named selections allow surfaces to be defined with a name and recall them. For the simulation of the output voltage of the sensing and harvesting piezoelectric parts, four named selections are needed. Two of them will be defined as the ground while the other two will be defined as the top electrode on the

piezoelectric material. The surfaces selected are surfaces of the piezoelectric material and not of the electrodes. The reason for this is that the electrodes are defined as mechanical elements and can not manage electrical variables in this model. The electrodes are modelled to define the structure in a realistic way, with same thickness and materials as will be used in the real harvester. The piezoelectric materials are defined as coupled field solid (solid226) and can manage both mechanical and piezoelectric parameters.

7.2.5 Analysis set up

For the modal analysis, a fixed support is defined at the end of the cantilever. For the harmonic analysis, in addition to the fixed support, it is necessary to the define the acceleration of the vibrating source by the direction and the intensity. In this simulation, the acceleration direction is defined as the Z axis, while the intensity is $1.96\frac{m}{s^2}$. It is also necessary to set the voltage on the ground electrodes as zero and set free voltage on top electrodes. To simulate open circuit conditions, an electrical load of $1G\Omega$ is connected between the ground electrodes and top electrodes.

7.2.6 Solution and results

From the modal analysis, the first three modes of vibration are found. The first natural frequency, which is of the greatest interest, is $40.75Hz$. Therefore a harmonic analysis is performed around this frequency and the output voltage is observed. In figure 7.3, it can be seen that the end tip of the cantilever, is the part under the greatest strain, while in figure 7.4 it is clear that the part near the clamped region is the more stressed. This means the output voltage of the sensing piezoelectric region will be high. From the harmonic analysis, the output voltage of the the harvesting and sensing piezo are found and shown in figure 7.5 and 7.6.It is observed that for both voltages, the output reaches a maximum at the resonant frequency of the device. Simulation results show that the sensing area of $3 \times 3mm$ is large enough to generate the voltage required by the SSPB circuit ($1.8V$).

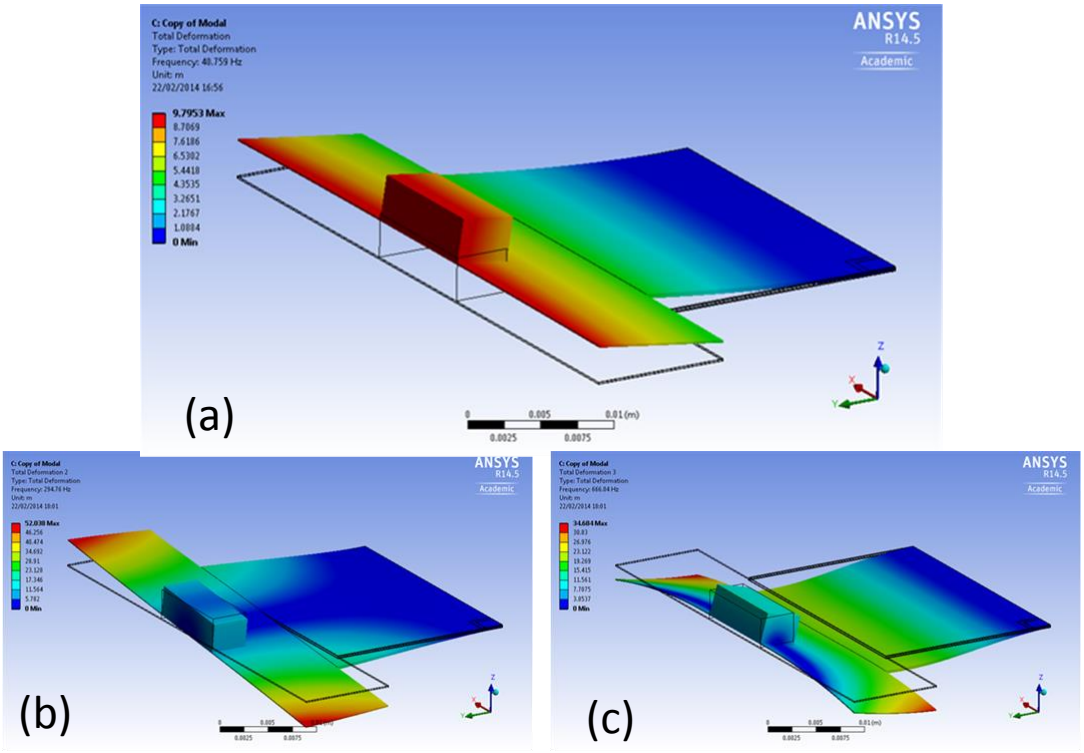

Figure 7.3. The first three natural frequencies of the energy harvester: (a)40.759Hz, (b) 294.76Hz, (c)666.04Hz

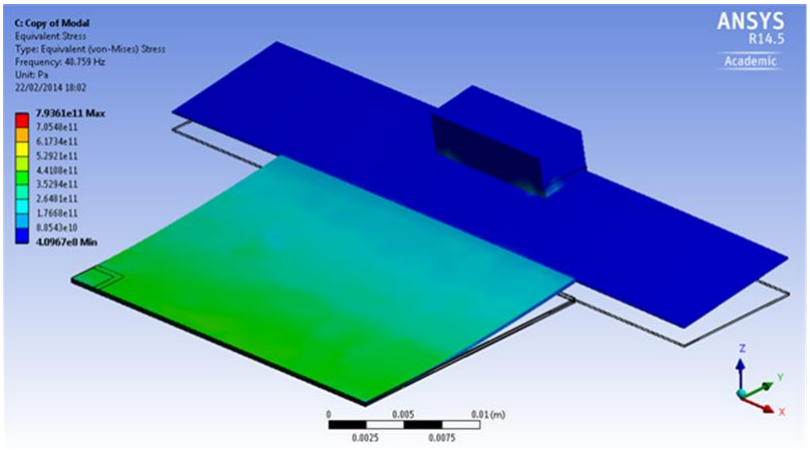

Figure 7.4. The equivalent stress illustrated on the cantilever.

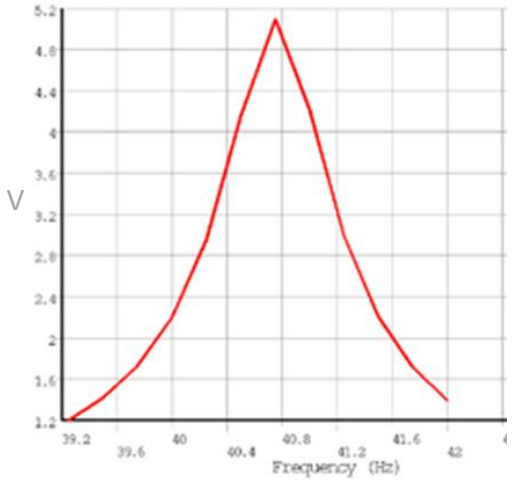

Figure 7.5. Simulated output voltage generated by the harvesting piezoelectric region.

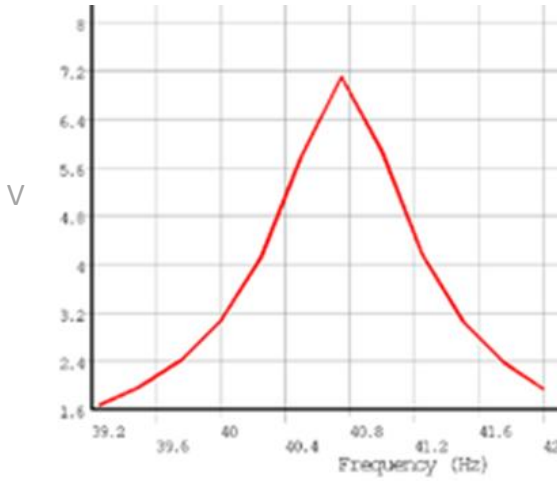

Figure 7.6. Simulated output voltage generated by the sensing piezoelectric region.

Chapter 8

Fabrication and testing of the piezoelectric energy harvester

In this chapter the fabrication and testing of the piezoelectric energy harvester are described.

8.1 Fabrication of the piezoelectric energy harvester

Screen printing was used to fabricate the piezoelectric energy harvester. This fabrication technology was chosen because it is low cost, low complexity and suitable for batch fabrication, which makes production faster. It is a thick film technology which involves the deposition of a paste on to a substrate by pushing it through a patterned screen. A screen is a woven mesh of threads made from nylon, polyester or stainless steel which are held in tension on a wooden or metal frame and coated with a UV-sensitive emulsion. Photolithography is then used to remove the emulsion in the required areas and create a pattern through which paste can pass.

The printing process involves pouring the paste on the top of the screen and positioning the substrate underneath. The screen is parallel with the substrate and there is usually a separation of $0.5mm$ between the two. A squeegee is then passed across the screen with a downwards pressure, which forces the paste through the patterned gaps and creates the desired pattern on the substrate. After printing the deposited films are dried at a relatively low temperature, usually around $150°C$, to remove organic carriers in the paste and produce a solid film on to which further layers can be printed. These are then fired at a higher temperature to sinter the films together and from a well bonded composite structure. Drying is required after each layer but firing can be carried out on multiple layers of a structure simultaneously.

Layers that are produced using thick film technology typically have a thickness within the range of $0.1 - 100\mu m$ [17]. The thickness is defined principally by the

thickness of the screen emulsion. To produce a complex structure, each material is printed with a different screen to produce a layer.

The piezoelectric paste uses lead zirconate titanate (PZT) as the active material. It is formulated by blending PZT-5H powders of various particle sizes with a binder [24]. The other layers use commercially available pastes supplied by Electro-Science Laboratories. The insulating dielectric layer is ESL4942. The pastes for the bottom and top electrodes are a gold paste (ESL8836) and a silver polymer paste (ESL1901-S) respectively. A polymer paste is used for the top electrode because this has a lower firing temperature and avoids the need for a second firing step, as discussed later. The substrate is stainless steel (type 430S17) which is compatible with the firing temperatures of all screen printable pastes used.

For the piezoelectric energy harvester the first layer is the substrate, which has a thickness of $110\mu m$. Two separate $10\mu m$ prints of ESL4942 provide a dielectric layer with thickness $20\mu m$. As it could be seen in figure 8.1, the dielectric layer covers totally the substrate surface. ESL8836 is then printed in a thickness of $10\mu m$ to provide the bottom electrodes. Figure 8.2 shows that parts of the gold printed are not connected to the harvesting and sensing grounds. These disconnected areas are designed to increase the thickness of the harvester where the top electrode will be printed. This, helps to avoid holes while the top electrode is printed. The piezoelectric paste is deposited in two separate prints of thickness $35\mu m$ to provide a $70\mu m$ thick layer of active material. Figure 8.3 shows that the piezoelectric areas printed are slightly bigger than the bottom electrodes areas.This helps to avoid short circuit between the top and bottom electrodes. Finally, ESL1901-S is deposited in a single print of thickness $10\mu m$ to produce the top electrode (figure 8.4). Each layer is dried at $140°C$ immediately after printing and fired at $850°C$. A firing step is carried out after the piezoelectric layer is printed to cure and sinter all printed layers at this point. Using a polymer paste for the top electrode avoids another firing step at high temperature after the piezoelectric paste is fired, and allows greater control over the conditions to which it is exposed. The total thickness of the printed device is $330\mu m$. The proof mass was not printed in so that it could be changed during experimentation.

After the device is printed the piezoelectric material is polarised. This is performed by simultaneously heating the devices to $200°C$ and applying an electric field of $4MVm^{-1}$. The temperature is maintained for 30 minutes and then the device is cooled. After 20 minutes, once the device has cooled, the electric field is turned off. A top-down view of the fabricated energy harvester is shown in figure 8.5.

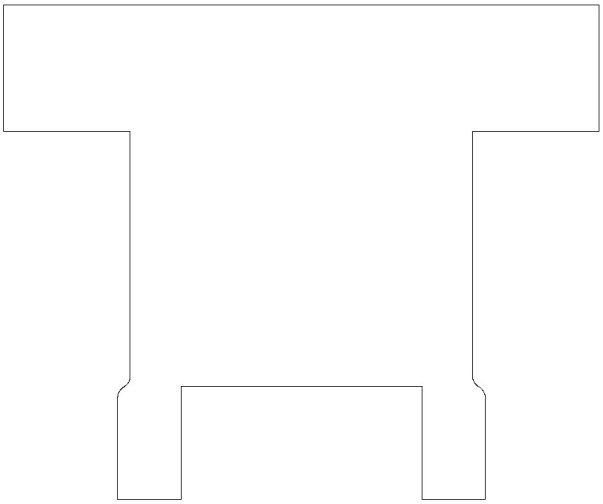

Figure 8.1. Pattern used to print the dielectric material un the substrate.

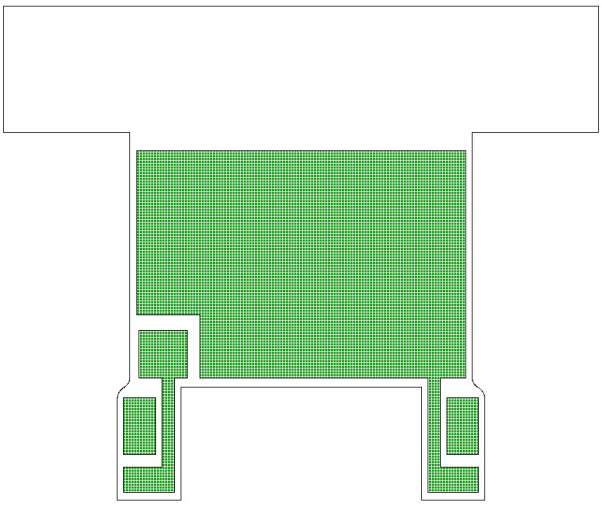

Figure 8.2. Pattern used to print the bottom electrode on the dielectric material (green).

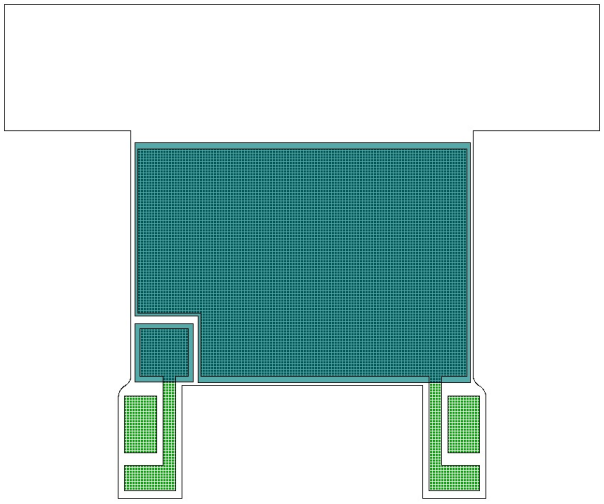

Figure 8.3. Pattern used to print the piezoelectric material on the bottom electrode (blu).

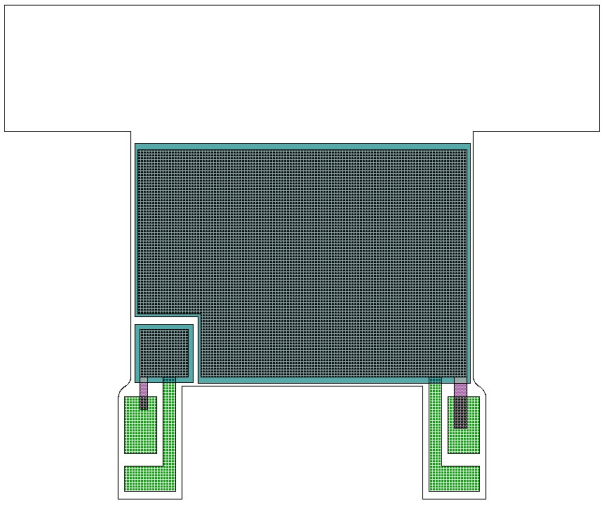

Figure 8.4. Pattern used to print the top electrode on the piezoelectric material (Violet).

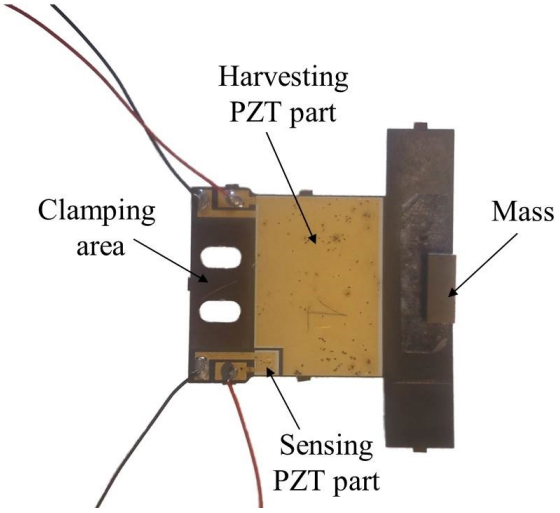

Figure 8.5. Top view of the T-shape piezoelectric harvester

8.2 Testing of the piezoelectric energy harvester

The SSPB circuit requires the sensing voltage and generator voltage waveforms to be in phase to accurately detect the peaks in the latter and maximise efficiency. However, because the two transduction elements have different areas and the same thickness they have different capacitances. The sensing element has a capacitance of $0.47nF$ while the generator element has a capacitance of $24.88nF$, resulting in a $66.24°$ phase shift when the voltage is measured using a low impedance measurement device. The harvester was tested on a Labworks ET-126 shaker, using a sinusoidal vibration with an RMS amplitude of 200 mg. Figure 8.6 shows the phase shift between sensing and generating voltages.

A common ground between the generator and sensing elements cancels the phase shift. However, this prevents proper operation of the SSPB circuit. Impedance matching was used instead to remove the phase shift. A $25nF$ capacitor was connected in parallel with the sensing element. Figure 8.7 shows the signals after the impedance was matched.

This shows that the sensing and generator voltages were brought into phase, improving the projected efficiency if the device were used with an SSPB circuit. The RMS open circuit voltage amplitude of the sensing and generator elements were measured at frequencies from 30 to 40 Hz. The results are shown in Figure 8.8.

The resonant frequency of the device was $36Hz$. This differs from the simulated resonant frequency, $40.75Hz$. This may be because the proof mass was attached to the device by hand and so its real position may differ from the simulation. Further, the clamping area was not modelled in the simulation and this could also have

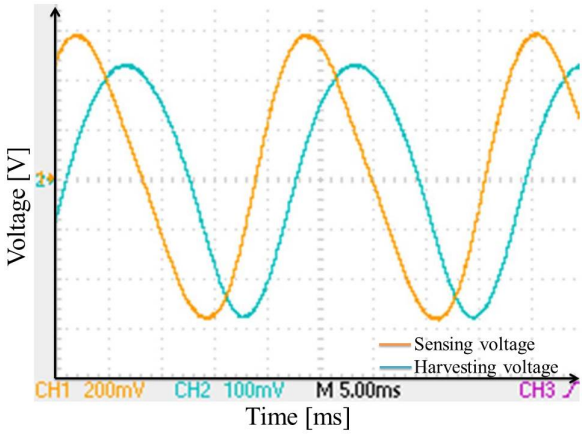

Figure 8.6. Experimentally measured waveforms showing piezoelectric open circuit voltage.

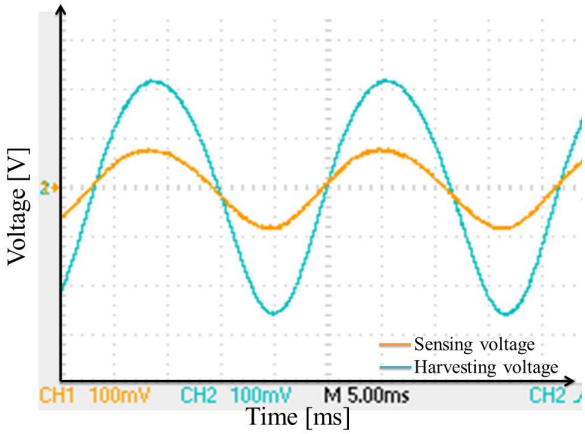

Figure 8.7. Experimentally measured waveforms showing piezoelectric open circuit voltage with a capacitance of 25 nF connected in parallel to the sensing PZT.

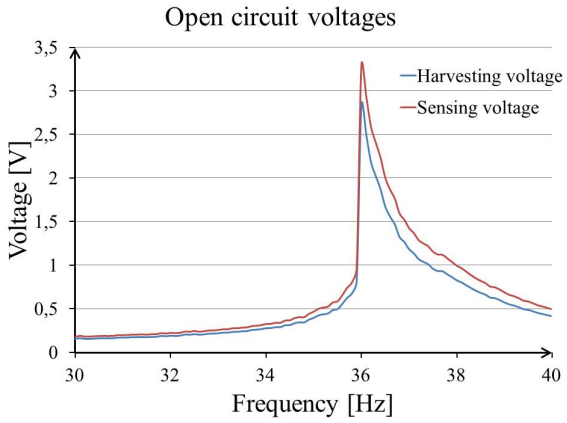

Figure 8.8. Open circuit voltages of the piezoelectric energy harvester.

affected results. Simulation of this novel device could be improved by employing transient analysis to examine the voltage waveforms and the phase shift between the two piezoelectric elements. In this project simulations were instead focused on predicting the voltage generated by the sensing and generator elements.

Chapter 9

Phase study of a piezoelectric energy harvester with integrated peak detection sensor for the SSPB circuit

The phase study between the harvesting voltage and the sensing voltage is studied and motivated in this chapter. The experimental results illustrated below may be different from those proposed in the previous chapter as are done after few months the harvester was fabricated. The results in the previous chapter are performed after just after the harvester was fabricated so after few months, the resonant frequency and the output voltage change slightly. Firstly an equivalent model is presented, secondly the harvester output is observed on the oscilloscope and finally observed in the data logger.

9.1 Equivalent model

Figure 9.1 shows an equivalent circuit of a piezoelectric energy harvester with electrical loads. The piezoelectric energy harvester was modelled as a sinusoid current source, I_p, connected in parallel with an internal resistor, R_p, and an internal capacitor, C_p. Electrical loads include a load resistor, R_L, and a load capacitor C_L. The relation between the output voltage, V, and the input current, I_p, can be represented by:

$$G(s) = \frac{V}{I_p} = \frac{R}{sRC + 1} \tag{9.1}$$

where:

$$R = \frac{R_p R_L}{R_p + R_L} \tag{9.2}$$

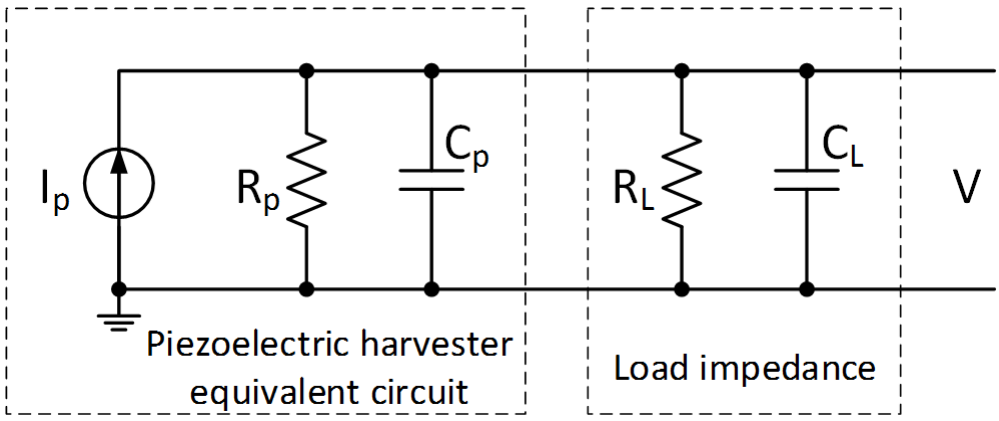

Figure 9.1. Equivalent circuit of a piezoelectric energy harvester with electrical loads.

is the equivalent resistance of the resistor of the piezoelectric layer, R_p, and the load resistor, R_L, connected in parallel and $C = C_p + C_L$ is the equivalent capacitance of the capacitor of piezoelectric layer, C_p, and the load capacitor, C_p, connected in parallel. Figure 9.2 shows the Bode phase plots of the transfer function with various values of RC as shown in equation 9.1.

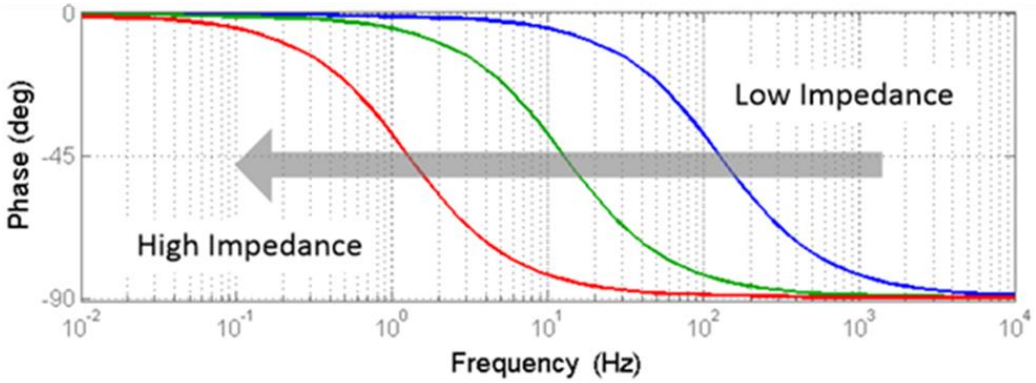

Figure 9.2. Bode phase plot of the transfer function as equation 9.1.

It was found that when the value of RC increases, the phase plot will shift to the left, i.e. the frequency where the phase is $-45°$ becomes lower. In other words, the phase of the transfer function becomes $-90°$ at lower frequencies when the value of RC is greater. To increase the value of RC, it is essential to increase either the load resistance, R_L, or the load capacitance, C_p.

9.2 Observation of the output voltage on an oscilloscope

The phase difference between the harvesting area and the peak detection sensor was first observed on an oscilloscope. Table 9.1 summarises values used in the model in this case. R_h and R_s are resistance of the harvesting area and the peak detection

Component	Value	Description
R_h	$100M\Omega$	Resistance of the harvesting area
C_h	$24.88nF$	Capacitance of the harvesting area
R_s	$100M\Omega$	Resistance of the peak detection sensor
C_s	$0.47nF$	Capacitance of the peak detection sensor
R_o	$1M\Omega$	Input resistance of the oscilloscope
C_o	$20pF$	Input capacitance of the oscilloscope

Table 9.1. Component values in the observation on an oscilloscope.

sensor, respectively. C_h and C_s are capacitance of the harvesting area and the peak detection sensor, respectively. These are all measured values. R_o and C_o are input resistance and capacitance of the oscilloscope (Tektronix TDS 2014), respectively. By using the values illustrated in table 9.1, the transfer functions of the harvesting area, $G_h(s)$, and the peak detection sensor, $G_s(s)$, can be calculated as:

$$\begin{aligned} G_h(s) &= \frac{9.901e5}{0.02465s+1} \\ G_s(s) &= \frac{9.901e5}{0.0004851s+1}. \end{aligned} \tag{9.3}$$

Figure 9.3 shows Bode phase plots of the transfer functions of $G_h(s)$ and $G_s(s)$.

It was found that there is a phase difference of 73° between the harvesting area and the peak detection sensor at the actual resonant frequency of 35.8 Hz. Experimentally, the phase difference between the harvesting area and the peak detection sensor was found to be 71.8° when observed in an oscilloscope as shown in Figure 9.4.

Therefore, the experimental result agrees with the simulation results according to the mathematical model. As suggested in the model, this phase difference was caused by the low load impedance and can be compensated by increasing the load impedance. Therefore, impedance matching was used to eliminate the phase difference by connecting a 25 nF capacitor in parallel with the peak detection sensor. The new transfer function of the peak detection sensor becomes:

$$G_{s-im}(s) = \frac{9.901e5}{0.002524s+1}. \tag{9.4}$$

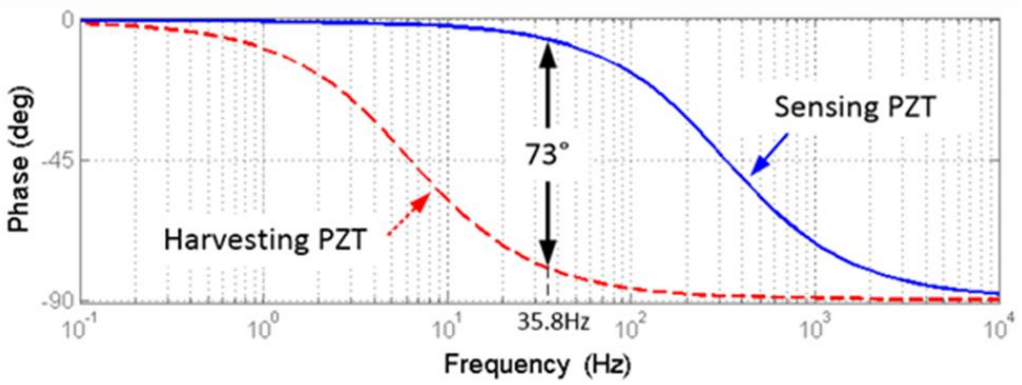

Figure 9.3. Bode phase plots of the transfer functions of the harvesting area and the peak detection sensor when observed in an oscilloscope.

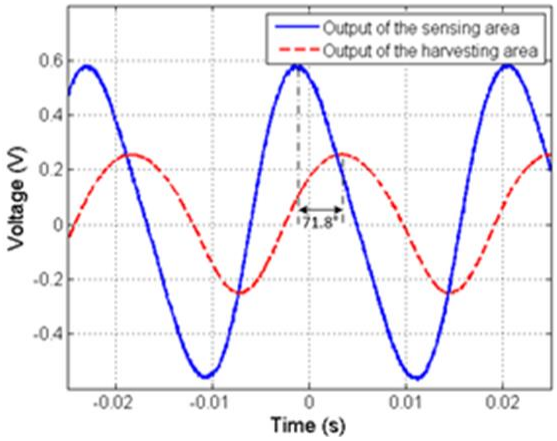

Figure 9.4. Measured phase difference between the harvesting area and the peak detection sensor when observed in an oscilloscope.

This is very similar to the transfer function of the harvesting area $G_h(s)$. Figure 9.5 shows bode phase plots of the transfer functions of the harvesting area and the peak detection sensor with the matched impedance.

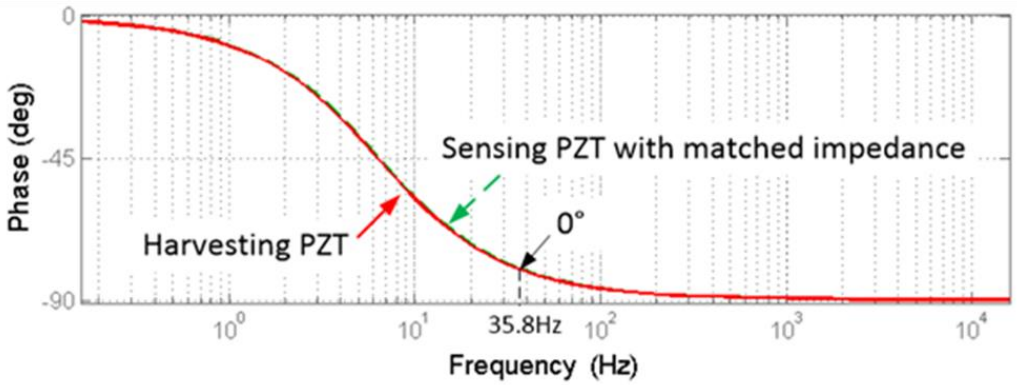

Figure 9.5. Bode phase plots of the transfer functions of the harvesting area and the peak detection sensor with the matched impedance when observed in an oscilloscope.

The two curves overlap and there is no phase difference at any frequency. Experimental results shown in figure 9.6 proved this.

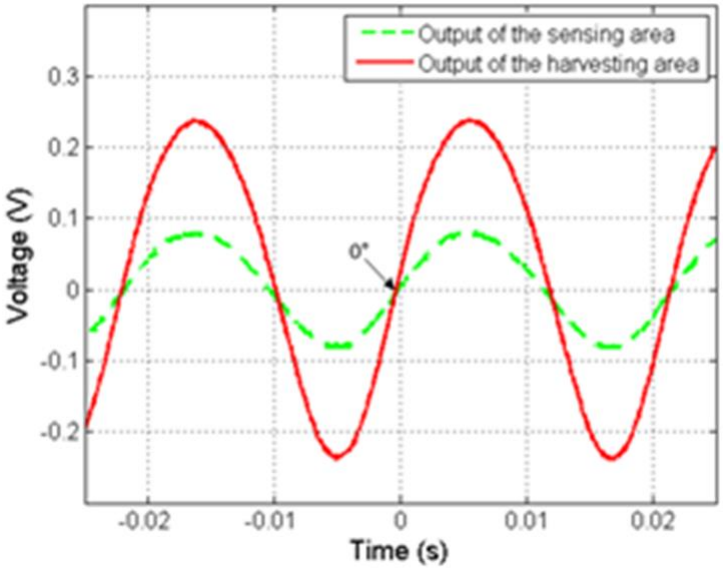

Figure 9.6. Measured phase difference between the harvesting area and the peak detection sensor with the matched impedance when observed in an oscilloscope.

Therefore, phase difference can be effectively eliminated by match impedance of the harvesting area and the peak detection sensor. It is worth mentioning that although there is no phase difference in the case of impedance matching, the amplitude

of the sensing signal is reduced due to the increased impedance.

9.3 Observation of the output voltage in data logger

The phase difference between the harvesting area and the peak detection sensor was then observed using a data logger which is open circuit to the input signal. The load resistance was infinite and the load capacitance was zero. Therefore, the total resistance, R, and the total capacitance, C, are the same as the internal resistance and capacitance of the piezoelectric areas, respectively. Transfer functions of the harvesting area, $G_h^{'}(s)$, and the peak detection sensor, $G_s^{'}(s)$, can be calculated as:

$$\begin{aligned} G_h(s) &= \frac{1e8}{2.488s+1} \\ G_s(s) &= \frac{1e8}{0.047s+1}. \end{aligned} \tag{9.5}$$

Figure 9.7 shows bode phase plots of the transfer functions of $G_h^{'}(s)$ and $G_s^{'}(s)$.

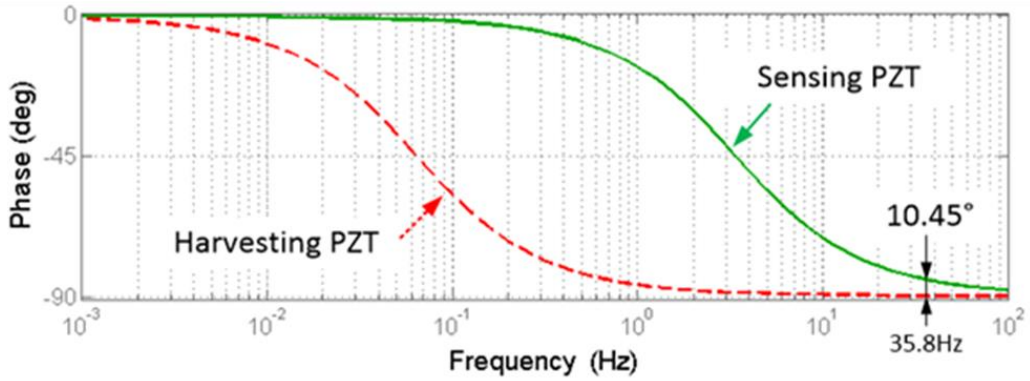

Figure 9.7. Bode phase plots of the transfer functions of the harvesting area and the peak detection sensor when connected to a data logger.

As the overall impedance became greater because of the increased load impedance, the phase plot shifted to the left. The phase difference between the harvesting area and the peak detection sensor at the actual resonant frequency (35.8 Hz) is only 10.45° in this case. Experimentally, the phase difference between the harvesting area and the peak detection sensor was found to be 13.3° when observed using a data logger as shown in figure 9.8. The result shows good agreement with the mathematical model.

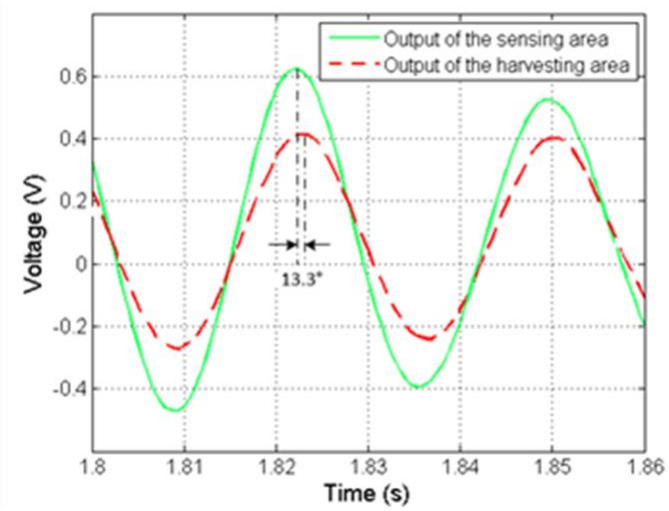

Figure 9.8. Measured phase difference between the harvesting area and the peak detection sensor when connected to a data logger.

Chapter 10

Conclusions

In the second part of the thesis, design, fabrication and test of a novel screen printed piezoelectric energy harvester for the single-supply pre-biasing circuit is presented. Like other active power conditioning circuits, the single-supply pre-biasing or SSPB circuit requires a sensing signal to detect the timing of the maximum deflection of the piezoelectric beam. The presented energy harvester design integrated peak sensors with the energy harvester in the same fabrication processes. The energy harvesting area and the peak detection sensor are electrically isolated to avoid interference.

To study the phase difference between the energy harvesting area and the peak detection sensor, a mathematical model was developed. Simulation results and experimental results were found to match each other. The difference in capacitance of these two areas resulted in a phase difference between them if the load impedance is low. In addition, since the harvesting area and the peak detection sensor do not share a common ground, the difference in capacitance leads to a phase shift between the two voltages. In the case of low load impedance, the phase difference can be successfully cancelled by matching the impedance of the peak detection sensor to the impedance of the harvesting area. Although the amplitude of the sensing signal can also be reduced by the impedance matching, it can be amplified in the peak detection circuit. Furthermore, if the load impedance is high, the Bode phase plot shifts to the left so that the energy harvester can work at a frequency where there is only a small phase difference between the two piezoelectric areas. In this case, a relatively small capacitor is required for impedance matching and the amplitude of the sensing signal will not be affected to dramatically.

Bibliography

[1] T. J. Kazmierski and S. Beeby. *Energy Harvesting Systems: Principles, Modeling and Applications*. Springer, New York, USA, 2011.

[2] Bosch Junkers. Minimaxxhydropower. `http://www.junkers.it/privati/prodotti/dettaglio_prodotto/scheda_prodotto_5059`, March 2014.

[3] D.-A. Wang and K.-H. Chang. Electromagnetic energy harvesting from flow induced vibration. *Microelectronics Journal*, 41(6):356–364, 2010.

[4] C.-Y. Wang, D.-A.and Chiu and H.-T. Pham. Electromagnetic energy harvesting from vibrations induced by karman vortex street. *Mechatronics*, 22(6):746–756, 2010.

[5] G.W. Taylor, J.R. Burns, S.A. Kammann, W.B. Powers, and T.R. Welsh. The energy harvesting eel: a small subsurface ocean/river power generator. *Oceanic Engineering, IEEE Journal of*, 26(4):539 –547, October 2001.

[6] D. A. Wang and H. H. Ko. Piezoelectric energy harvesting from flow-induced vibration. *Journal of Micromechanics and Microengineering*, 20(2), 2010.

[7] Dung-An Wang, Huy-Tuan Pham, Chia-Wei Chao, and Jerry M Chen. A piezoelectric energy harvester based on pressure fluctuations in kármán vortex street. In *Proceedings World Renewable Energy Congress 2011*, 2011.

[8] The Chicago Faucet Company. Self sustaining power supply. `http://www.chicagofaucet.com/pdf/CF2002.pdf`, March 2014.

[9] Enrico Zenerino, J.G. Detoni, D. Boero, A. Tonoli, and M. Chiaberge. *Trade-off Analysis and Design of a Hydraulic Energy Scavenger*, chapter 18, pages 467–486. InTech, 2012.

[10] F. Clark. Showerhead with turbine driven light source. `http://www.google.com/patents/US7387401`, June 2008. US Patent 7,387,401.

[11] Nand Kishor, R.P. Saini, and S.P. Singh. A review on hydropower plant models and control. *Renewable and Sustainable Energy Reviews*, 11(5):776 – 796, 2007.

[12] Matei Vinatoru, Eugen Iancu, Camelia Maican, and Gabriela Canureci. Control system for kaplan hydro-turbine. In *Proceedings of the 4th WSEAS/IASME international conference on Dynamical systems and control*, pages 73–78, Stevens Point, Wisconsin, USA, 2008. World Scientific and Engineering Academy and Society (WSEAS).

[13] Nand Kishor, S.P. Singh, and A.S. Raghuvanshi. Dynamic simulations of hydro turbine and its state estimation based lq control. *Energy Conversion and Management*, 47(18-19):3119–3137, 2006.

[14] Jesús De Andrade, Christian Curiel, Frank Kenyery, Orlando Aguillón, Auristela Vásquez, and Miguel Asuaje. Numerical investigation of the internal flow in a banki turbine. *International Journal of Rotating Machinery*, 2011, 2011.

[15] C.A. Mockmore and F. Merryfield. The banki water turbine. *Bullettin series*, 1111(25), 1949.

[16] E. F. Fuchs and M. A. S. Masoum. *Power conversion of renewable energy systems*, pages 540–541. Springer, New York, USA, 2011.

[17] S P Beeby, M J Tudor, and NM White. Energy harvesting vibration sources for microsystems applications. *Measurement science and technology*, 17(12):R175, 2006.

[18] S. Vijaya. *Piezoelectric Materials and Devices: Applications in Engineering and Medical Sciences*. Taylor & Francis, 2012.

[19] Hyeoungwoo Kim, Shashank Priya, Harry Stephanou, and Kenji Uchino. Consideration of impedance matching techniques for efficient piezoelectric energy harvesting. *Ultrasonics, Ferroelectrics and Frequency Control, IEEE Transactions on*, 54(9):1851–1859, 2007.

[20] James Dicken, Paul D Mitcheson, Ivan Stoianov, and Eric M Yeatman. Power-extraction circuits for piezoelectric energy harvesters in miniature and low-power applications. *Power Electronics, IEEE Transactions on*, 27(11):4514–4529, 2012.

[21] S. Beeby and N. White. *Energy Harvesting for Autonomous Systems*. Artech House, Incorporated, 2010.

[22] ADT Elliott, D Zhu, SP Beeby, and PD Mitcheson. Multilayer piezoelectric energy harvesting using single supply pre-biasing for maximum power generation. In *PowerMEMS*, 2012.

[23] Dibin Zhu, Stephen P Beeby, Michael J Tudor, and Nick R Harris. A credit card sized self powered smart sensor node. *Sensors and Actuators A: Physical*, 169(2):317–325, 2011.

[24] RN Torah, SP Beeby, MJ Tudor, and NM White. Thick-film piezoceramics and devices. *Journal of Electroceramics*, 19(1):97–112, 2007.

List of Figures

List of Tables